

Direct observation of ultrafast many-body electron dynamics in a strongly-correlated ultracold Rydberg gas

Nobuyuki Takei^{1,2,3,*}, Christian Sommer^{1,2,3,*}, Claudiu Genes^{3,4}, Guido Pupillo^{3,5}, Haruka Goto¹, Kuniaki Koyasu^{1,2,3}, Hisashi Chiba^{1,3,6}, Matthias Weidemüller^{3,7,8}, and Kenji Ohmori^{1,2,3}
¹*Institute for Molecular Science, National Institutes of Natural Sciences, Myodaiji, Okazaki 444-8585, Japan*
²*SOKENDAI (The Graduate University for Advanced Studies), Okazaki 444-8585, Japan*
³*CREST, Japan Science and Technology Agency, Kawaguchi 332-0012, Japan*
⁴*Institut für Theoretische Physik, Universität Innsbruck, Technikerstrasse 25, A-6020 Innsbruck, Austria*
⁵*IPCMS (UMR 7504) and ISIS (UMR 7006), University of Strasbourg and CNRS, 67000 Strasbourg, France*
⁶*Faculty of Engineering, Iwate University, 4-3-5 Ueda, Morioka 020-8551, Japan*
⁷*Physikalisches Institut, Universität Heidelberg, Im Neuenheimer Feld 226, 69120 Heidelberg, Germany*
⁸*Hefei National Laboratory for Physical Sciences at the Microscale and Department of Modern Physics, and CAS Center for Excellence and Synergetic Innovation Center in Quantum Information and Quantum Physics, University of Science and Technology of China, Hefei, Anhui 230026, China*

*These authors contributed equally to this work.

(Dated: May 30, 2022)

Many-body interactions govern a variety of important quantum phenomena ranging from the emergence of magnetism and superconductivity in condensed matter to solvent effects in chemistry. Understanding those interactions beyond mean field is one of the holy grails of modern sciences. Atomic, molecular, and optical physics with advanced laser technologies has recently emerged as a new platform to study quantum many-body systems [1]. One of its latest developments is the study of long-range interactions among ultracold particles, where dipolar quantum gases [2, 3], ion crystals [4, 5], and polar molecules [6, 7] allow to reveal the effects of many-body correlations in and out of equilibrium. Rydberg atoms distinguish themselves by their large dipole moments and tunability of the strength and nature of dipolar interactions [8]. Most of ultracold Rydberg experiments have been performed with narrow-band lasers in a regime referred to as Rydberg blockade [8–10] in which only one Rydberg excitation can exist in an atomic ensemble whose size is typically on the order of several micrometers (μm). Here we demonstrate the realization of an ultracold Rydberg gas in a complementary regime, where electronic coherence in rubidium (Rb) atoms is created using a broadband picosecond (ps) laser pulse, thus circumventing the Rydberg blockade to induce strong many-body correlations. The effects of long-range Rydberg interactions have been investigated by time-domain Ramsey interferometry with attosecond precision. This approach allows for the real-time observation of coherent and ultrafast many-body dynamics in which the electronic coherence is modulated by the interaction-induced correlations. The modulation evolves more rapidly than expected for two-body correlations by several orders of magnitude. We have actively controlled such ultrafast many-body dynamics by tuning the principal quantum number and the population of the Rydberg state. The observed Ramsey interferograms are well reproduced by a theoretical model beyond the mean-field approximation, which can be relevant to other similar many-body phenomena in condensed matter physics and chemistry. Our new approach opens a new avenue to observe and manipulate nonequilibrium dynamics of strongly-correlated quantum many-body systems on the ultrafast timescale.

A Rydberg atom is an atomic giant where an electron moves in a macroscopic orbital whose size could range from sub- μm to several tens of μm [11, 12]. The resulting large dipole moments yield a long-range interaction $U(r)$ between a pair of Rydberg atoms separated by r . These interactions shift the energy levels of all the atoms surrounding a given Rydberg-excited atom, so that additional Rydberg excitations by narrow-band continuous-wave (CW) lasers are blocked for $U(r)$ larger than the atomic and laser line-widths, respectively. This is referred to as Rydberg blockade [8–10]. Novel studies on the Rydberg blockade are emerging recently from a viewpoint of its possible applications to universal logic gates in quantum information processing [8, 13–17]. The Rydberg blockade has also turned out to be an outstanding new resource to investigate many-body problems [18]; pi-

oneering experiments have demonstrated first examples of spatial [19–21] and temporal [22–25] correlations in optical traps in the blockade regime. Ultimately, the blockade determines a maximal interaction strength or equivalently a smallest interatomic separation r_B usually of the order of several μm .

Using a broadband ps laser pulse, the Rydberg blockade can be circumvented to increase the two-body Rydberg interaction strength by one–two orders of magnitude. This drastic enhancement allows us to access a strongly interacting regime where the characteristic interaction energy is several orders of magnitude larger than the average kinetic energy. The resulting many-body interaction is clearly manifested in a dephasing on the ultrafast ps timescale, which we measure directly in the time domain by Ramsey interferometry with at-

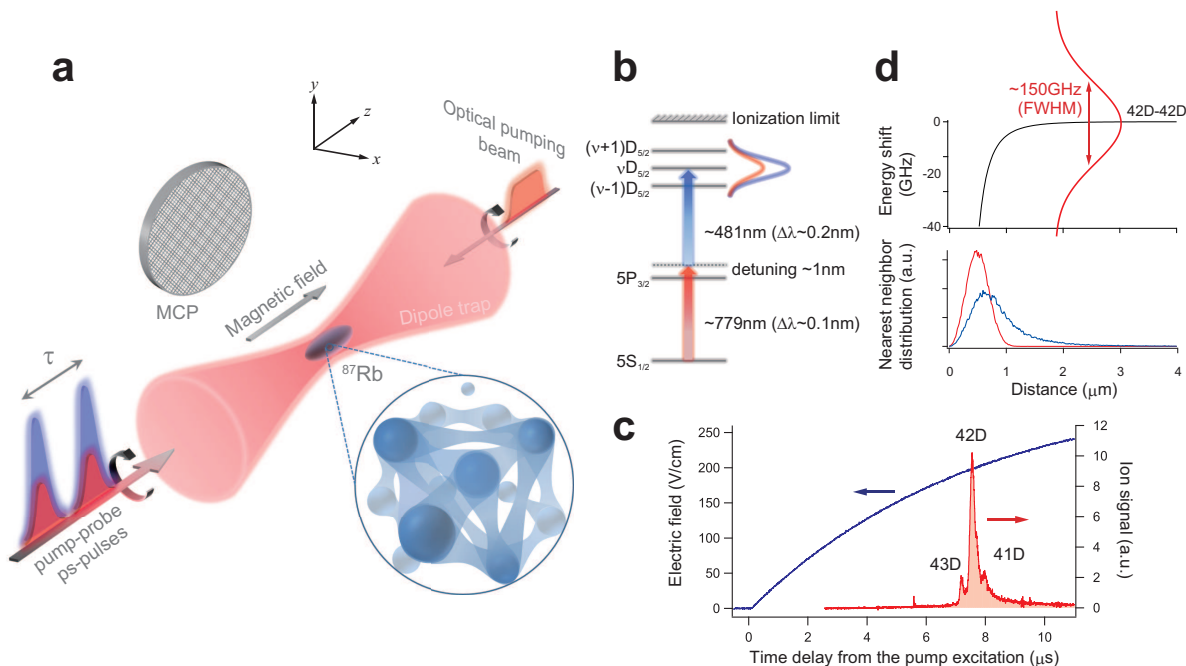


FIG. 1: Schematic diagram of the experimental setup and Rydberg excitation. **a**, A sketch of the experimental setup. The dipole-trap laser is turned off $2\ \mu\text{s}$ before the irradiation of the ps pulses to avoid $2+1$ multiphoton ionization induced by a combination of the ps pulses and the trapping laser beam. **b**, Two-photon pump (probe) excitation of the Rb atom to its Rydberg-states. **c**, The Rydberg states can be resolved by field ionization with a slowly ramped electric field (see Methods and Supplementary Information). Here, the Rydberg population and estimated atom density were $1.2 \pm 0.1\ \%$ and $\sim 4 \times 10^{10}\ \text{cm}^{-3}$, respectively (see Methods for this density estimation). The small peak around $5.6\ \mu\text{s}$ could be assigned to free ions generated by population redistribution [32] and/or direct multiphoton ionization. **d**, Sketch of the interaction accompanied by a plot of the nearest-neighbor distribution for the peak density of $n = 1.3 \times 10^{12}\ \text{cm}^{-3}$ (red trace) and the averaged density over the whole atoms (blue trace) estimated for the present ensemble of the Rb atoms (see Methods for this density estimation). At the peak density the average nearest-neighbor distance is given by $0.5\ \mu\text{m}$, whereas for the averaged density we obtain $0.87\ \mu\text{m}$.

tosecond precision [26]. The observed ultrafast dynamics is successfully described by a theoretical model beyond mean-field approximation that necessitates the inclusion of interactions among more than several tens of Rydberg atoms. While ps laser pulses have been previously used to observe electronic wave-packets in isolated Rydberg atoms [27] and the dephasing due to two-body interactions [22, 23, 28], we now exploit them to explore how coherent dynamics evolves in a strongly-interacting many-body Rydberg system. The effect of many-body interactions on coherent dynamics has recently been investigated with polar molecules in an optical lattice trap [6]. The timescale of the interaction in this polar-molecule experiment is ~ 19 milliseconds (ms), shorter than that of the trap-loss decay of the molecules by three orders of magnitude. The interaction timescale in our current experiment is ~ 1 nanosecond (ns) and is shorter than the timescales for collisions and radiative decay by three and four orders of magnitudes, respectively. The interaction timescale is thus much shorter than the decay lifetime in both of these experiments. The interaction

timescale should also be shorter than the decoherence timescale to observe the effect of many-body interactions on coherent dynamics. The interaction timescale ~ 19 ms in the polar-molecule experiment is comparable with the timescale ~ 80 ms of single-particle decoherence induced by the trap-potential inhomogeneity. In our experiment, on the other hand, the interaction timescale ~ 1 ns is about three orders of magnitude shorter than the timescale of single-particle decoherence induced mainly by Doppler broadening, which is ~ 1.5 microseconds (μs) at a temperature $\sim 70\ \mu\text{K}$ estimated for our Rydberg gas (see Methods for this temperature estimation). The combination of ultrafast and ultracold approaches is thus effective in isolating the observation and control of coherent dynamics from decoherence.

Figure 1a shows the schematics of our experimental setup. A cold ensemble of ^{87}Rb atoms is prepared in an optical dipole trap with its temperature and highest peak atom-density estimated to be $\sim 70\ \mu\text{K}$ and $\sim 1.3 \times 10^{12}\ \text{cm}^{-3}$, respectively, in the frozen gas regime [29, 30] (see Methods for these temperature and

density estimations). The atoms are optically pumped to the hyperfine state $F=2$, $m_F=+2$ of the ground state $5S_{1/2}$ and then excited to Rydberg states via a two-photon transition using broadband ps laser pulses with their center-wavelengths tuned to ~ 779 nm and ~ 481 nm (Fig. 1b), hereafter referred to as the IR and blue pulses, respectively. The dipole-trap laser is turned off $2 \mu\text{s}$ before the irradiation of the IR and blue pulses to avoid $2+1$ multiphoton ionization induced by a combination of the IR and blue pulses and the trapping laser beam. The IR and blue pulses and the optical pumping beam are circularly polarized in the same direction with respect to the magnetic field, suppressing excitations to the S Rydberg states, so that the state $\nu D_{5/2}$, $m_J=+5/2$ is mostly populated, where ν is a principal quantum number. The maximum population of the νD states in the present experiment is not larger than 5% in order to suppress photo-ionization. More details of the atom preparation, estimation of the atom density and the temperature, and the Rydberg excitation are described in Methods.

The bandwidth of our Rydberg excitation with the IR and blue pulses is about 150 GHz (FWHM) and is thus much larger than that of the CW and ns pulsed lasers employed in previous experiments [28, 31, 32]. The bandwidth is determined from field-ionization spectra such as presented in Fig. 1c (see Supplementary Information). Here, the Rb atoms are irradiated with the IR and blue pulses tuned to the $42D_{5/2}$ state, which is the main target-state of the current experiment. This field-ionization spectrum indicates that the bandwidth of the two-photon excitation is larger than the energy separation of neighboring Rydberg states and is accordingly wide enough to remove the Rydberg blockade. As schematically shown in the upper panel of Fig. 1d, our ps laser pulses can excite a pair of Rb atoms simultaneously to the Rydberg states $\nu = 42$ even at interatomic distances shorter than $1 \mu\text{m}$. Our nearest neighbor distance between Rydberg atoms can therefore be much shorter than those of the previous CW, ns, and sub-ns experiments, which were $\sim 3\text{--}4 \mu\text{m}$ [21, 28, 31, 32]. The two-body interaction energy of the $42D_{5/2}$ state changes by one–two orders in going from 3 to $1 \mu\text{m}$.

The interaction among the Rydberg atoms is observed by time-domain Ramsey interferometry with a pair of the two-photon excitations hereafter referred to as the “pump” and “probe” excitations whose delay was stabilized on the attosecond timescale with our homemade optical interferometer [33]. By scanning the delay time τ between the pump and probe excitations on the attosecond timescale, we measure the interferogram of the population integrated over all the Rydberg states that remains after the probe excitation and is subsequently detected by field ionization. We have employed two different methods of the field ionization between the measurements of this interferogram and the field-ionization

spectrum which is shown in Fig. 1c. Details of the field ionization are described in Methods and Supplementary Information. For the excitation tuned to the $42D_{5/2}$ state as shown in Fig. 1c, a single Rydberg state $|\nu\rangle$ with $\nu = 42$ is predominantly populated. In the absence of interactions, this population $P_\nu(\tau)$ is given by

$$P_\nu(\tau) \propto 1 + \cos(E_\nu\tau/\hbar), \quad (1)$$

displaying oscillations at the frequency E_ν/h , where E_ν is the energy of the Rydberg state $|\nu\rangle$ [26], and \hbar is the Planck constant h divided by 2π . This oscillation is identical to the temporal oscillation of the Rydberg state $|\nu\rangle$ except that the real time t is replaced by the pump-probe delay τ . Therefore the oscillation seen in our Ramsey interferogram for $\nu = 42$ almost corresponds to the oscillation of the Rydberg state $|\nu = 42\rangle$ and to the recurrence motion of an electronic wave-packet, which is composed of the 5S and Rydberg state $|\nu = 42\rangle$ superposed coherently by the IR and blue pulses.

In a simplified mean-field approach, the effect of interactions is to shift the energy of the level $|\nu\rangle$ and therefore to modify the oscillation period of $P_\nu(\tau)$. This results in an accumulated phase-shift in the interferogram after a time τ . In addition, as the atoms are randomly distributed in the ensemble, their energy levels E_ν are shifted randomly by interactions, making their interferograms oscillate with different periods. The measured interferogram is, therefore, the superposition of those many interferograms of different periods, so that its contrast is expected to decay as a function of time due to Rydberg interactions. Figures 2a, b, and c show examples of the interferograms for the $42D_{5/2}$ state with a population of $3.3 \pm 0.1\%$. As is mentioned above, the oscillation in these interferograms corresponds to the ultrafast recurrence motion of the electronic wave-packet with a period of about 1 femtosecond (fs). In each of these interferograms, we measured the field-ionization signals of two atomic ensembles with different peak densities estimated to be $\sim 1.3 \times 10^{12} \text{ cm}^{-3}$ and $\sim 4 \times 10^{10} \text{ cm}^{-3}$ alternately to suppress systematic uncertainties, scanning τ in steps of ~ 30 attoseconds (see Methods for these density estimations). We obtained the contrasts and phases of the measured interferograms by sinusoidal fittings, as shown in Figs. 2a–c. Figure 2d shows that the contrast is approximately constant for τ up to ~ 500 ps for the lower-density ensemble, indicating that interaction effects are negligibly small. This result is consistent with the interaction strength estimated from the present atom-density and the two-atom potential curve presented in Supplementary Information. Hereafter we assume that many-body interactions are negligible in this lower-density ensemble, which is hereafter taken to be a reference for measuring the contrast decay and the phase-shift that may be induced by the interactions in the higher-density ensemble.

For the higher-density ensemble, on the other hand,

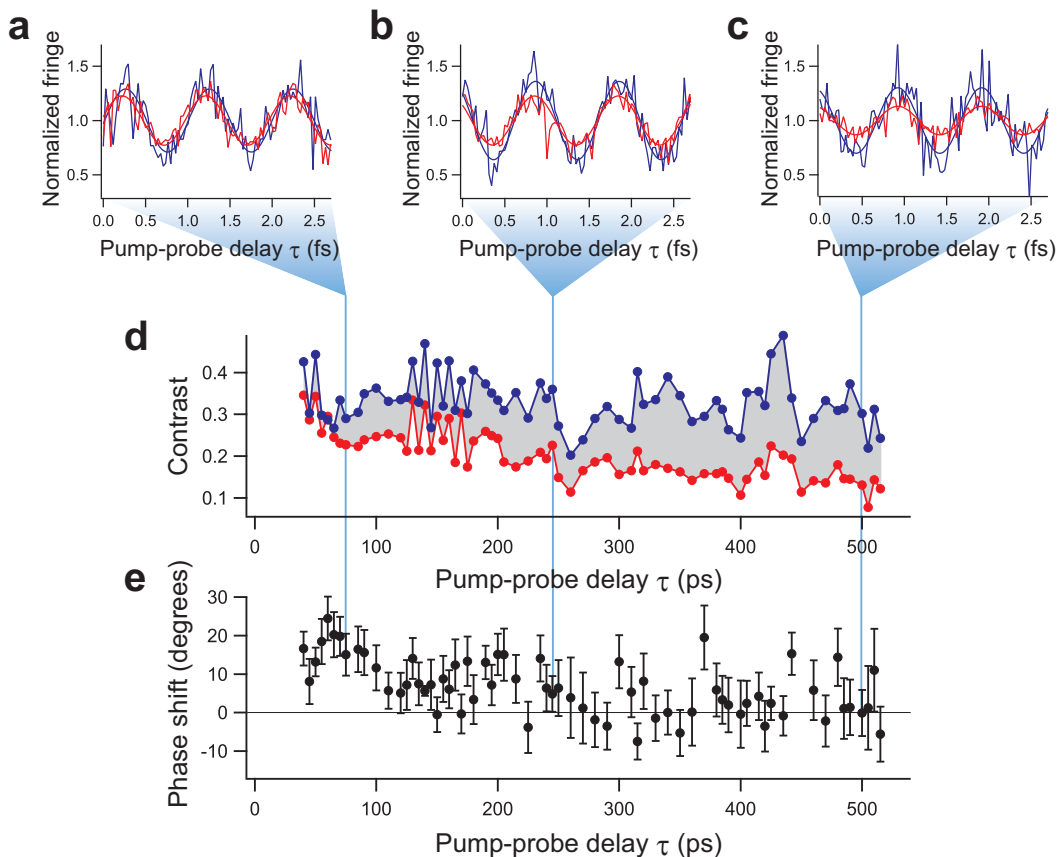


FIG. 2: **Ramsey interferogram for the 42D state.** **a**, **b** and **c**, The field-ionization signals for the higher-density (red traces) and the lower-density (blue traces) ensembles are plotted as functions of the pump-probe delay τ scanned over a range of ~ 3 femtoseconds (fs) around 75 ps, 245 ps, and 500 ps, showing clear interferograms. The signal intensities are normalized by the mean value of the sinusoidal function fitted to each interferogram. The origin of the pump-probe delay $\tau = 0$ is arbitrary and is taken to be the left edge of each figure. **d**, The contrasts of these interferograms are plotted as functions of τ . The oscillatory structures as functions of τ could be partly attributable to the recurrence motion of a wave-packet composed of the 42D and its neighboring Rydberg states (see the field-ionization spectrum shown in Fig. 1c). The shortest period of this recurrence motion is evaluated from their level-spacing to be ~ 10 ps, which is not resolved in these plots. The contrast decays clearly as a function of τ for the higher-density ensemble, whereas for the lower-density one a decay is not visible. **e**, The phase-shift of the higher-density ensemble from the lower-density one is plotted as a function of τ . The oscillatory structure as a function of τ is partly attributable to the wave-packet motion.

the contrast clearly decays as a function of τ . Figure 2e shows the phase-shift of the higher-density ensemble from the lower-density one. It is seen that the phase-shift also changes as a function of τ . The offset of this phase-shift at $\tau = 0$ is most likely resultant of differences in AC-Stark shifts between the higher- and lower-density ensembles (see Methods and Supplementary Information).

Figures 3 and 4 show the results of extensive measurements of the contrast ratio between the two different densities given above, hereafter referred to as “Ramsey contrast”, and the phase-shift for the $42D_{5/2}$ state. These results are plotted as functions of τ for the two different Rydberg populations of $1.2 \pm 0.1\%$ and $3.3 \pm 0.1\%$. We find that, even though the Rydberg population is no more than a few percent, the Ramsey-contrast decays

and phase-shifts are accumulated as functions of time in the higher-density ensemble. In other words, the motion of the electronic wave-packet mentioned above is modulated. These results signal that the effects of interactions are significant.

We develop a model to analyze the dynamics behind these observations, where each atom is described by a two-level system. We consider a ground state $|g\rangle$ and an excited Rydberg state $|e\rangle$ with energies E_g and E_e , respectively. This assumption should be reasonable as the contribution of the neighboring Rydberg levels is small for the $42D_{5/2}$ state, as seen from the field-ionization spectrum shown in Fig. 1c. The effect of the two-photon driving on an atom is contained in the single-atom uni-

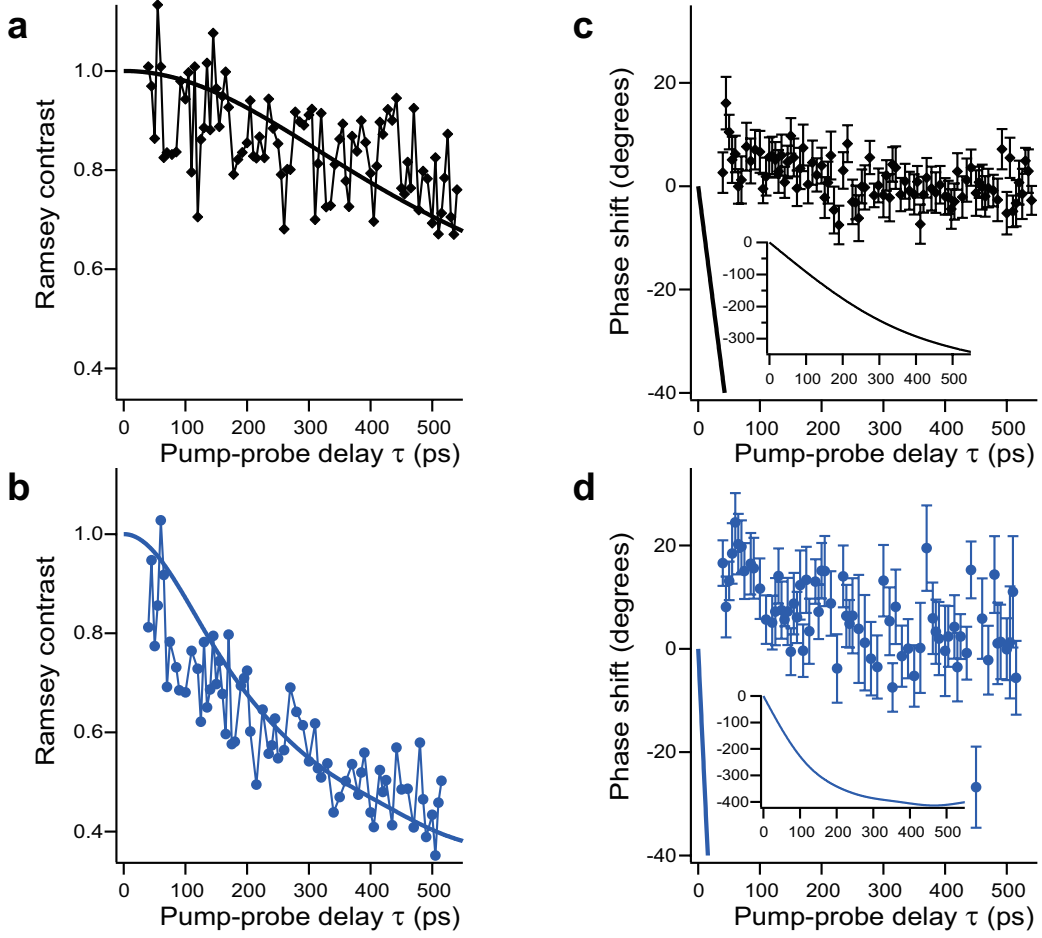


FIG. 3: **Mean-field-model analysis of the Ramsey contrast and the phase shift.** The black-diamond-shaped and blue-circle data-points show the Ramsey contrasts (**a** and **b**) and the phase-shifts (**c** and **d**) measured with the population of the $42D_{5/2}$ state being $\sim 1.2\%$ (**a** and **c**) and $\sim 3.3\%$ (**b** and **d**), respectively. In **a** and **b**, the Ramsey contrasts simulated by mean-field theory (black and blue solid lines) are compared with the measured ones. Similarly, the measured and simulated phase-shifts are compared in **c** and **d**. The insets in **c** and **d** show the whole features of the simulated phase-shifts by reducing their vertical scalings. The zero-delay offset of the simulated phase-shift is arbitrary and set to 0 degree. The interaction strength is limited below 75 GHz, which is the bandwidth (half width half maximum) of the pump excitation, and the peak atom density is set to $\sim 1.3 \times 10^{12} \text{ cm}^{-3}$ in these simulations.

tary transformation

$$A = \begin{pmatrix} c_g & ic_e \\ ic_e^* & c_g^* \end{pmatrix},$$

where c_g and c_e are the amplitudes of the $|g\rangle$ and $|e\rangle$ states, respectively. The N -atom wave function is initially assumed to be a product of independent single-atom wave functions $|g\rangle^{\otimes N}$. The dynamics during the Ramsey measurement is then described by the time-evolution of the N -atom wave-function $|\Psi(\tau)\rangle_N$

$$|\Psi(\tau)\rangle_N = A^{\otimes N} \exp\left(-i\frac{\hat{H}}{\hbar}\tau\right) A^{\otimes N}|g\rangle^{\otimes N}. \quad (2)$$

The measurement consists of three stages: (i) the pump excitation described by $A^{\otimes N}$, (ii) an evolution with a

many-body Hamiltonian \hat{H} , and (iii) the probe excitation $A^{\otimes N}$. The experimental observable is the number of Rydberg excited atoms detected as a time-dependent signal $P(\tau) = \langle \Psi(\tau) | \hat{P} | \Psi(\tau) \rangle_N$, which is the expectation value of the sum of projection operators $\hat{P} = \sum_{j=1}^N \hat{P}_j$, where $\hat{P}_j \equiv |e\rangle_j \langle e|_j / N$ measures the population in the Rydberg state for atom j normalized to the total atom number N .

The N -atom Hamiltonian reads

$$\hat{H} = \sum_{j=1}^N (E_g |g\rangle_j \langle g|_j + E_e |e\rangle_j \langle e|_j) + \sum_{j=1}^{N-1} \sum_{i>j}^N \hat{U}(r_{ij}) |e\rangle_j \langle e|_i \langle e|_i \langle e|_j + \dots, \quad (3)$$

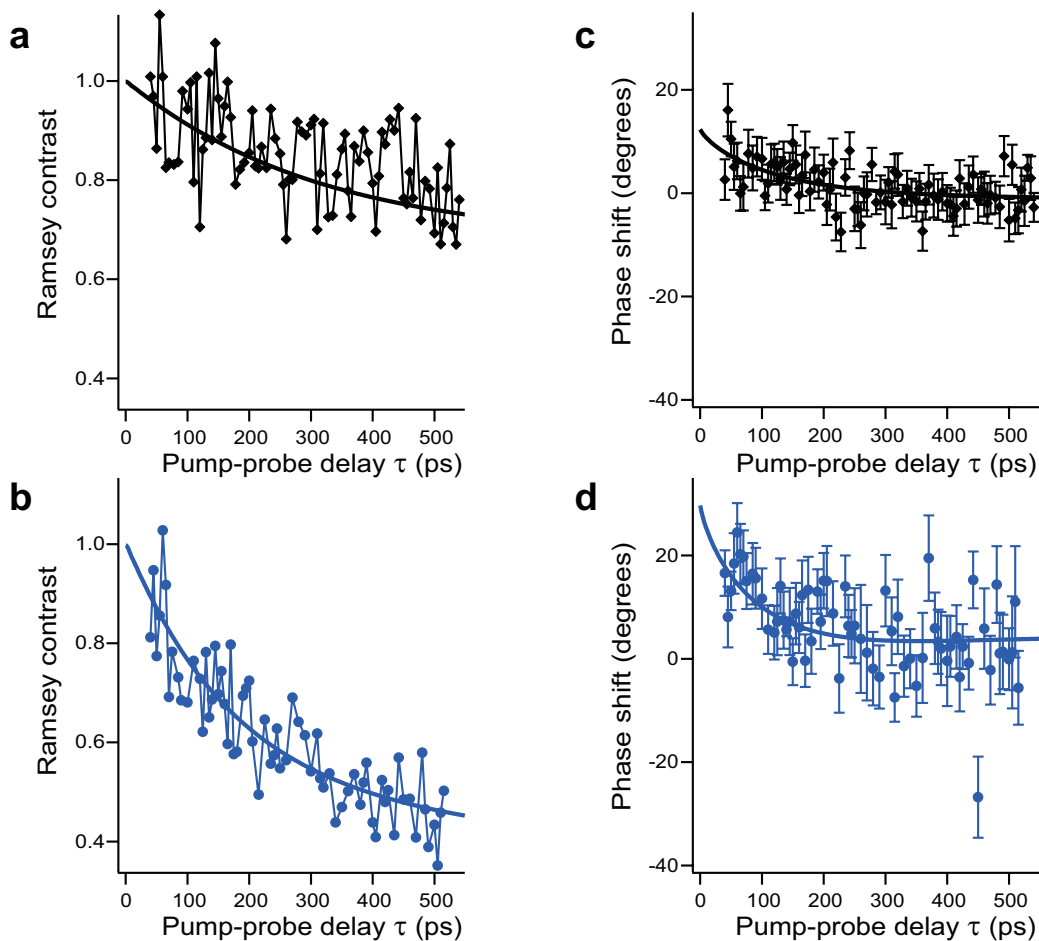


FIG. 4: **ARM analysis of the Ramsey contrast and the phase shift.** The black-diamond-shaped and blue-circle data-points show the Ramsey contrasts (**a** and **b**) and the phase-shifts (**c** and **d**) measured with the population of the $42D_{5/2}$ state being $\sim 1.2\%$ (**a** and **c**) and $\sim 3.3\%$ (**b** and **d**), respectively. In **a** and **b**, the Ramsey contrasts simulated by ARM (black and blue solid lines) are compared with the measured ones. Similarly, the measured and simulated phase-shifts are compared in **c** and **d**. The interaction strength in these simulations is limited below 75 GHz, which is the half width half maximum of the pump excitation, and the peak atom density is set to $\sim 1.3 \times 10^{12} \text{ cm}^{-3}$ in these simulations.

where only interactions $\hat{U}(r_{ij})$ between atoms in the Rydberg states are considered. This is justified on the ps timescale of the current measurement since these interactions provide coupling strengths on the order of GHz for μm separations. These interactions are much larger than those between ground-state atoms and ground- and Rydberg-state atoms, which are on the order of kHz and MHz for μm separations, respectively.

Solving the many-body dynamics of Eqs. (2) and (3) provides a formidable task, which usually requires approximate numerical or analytical techniques. Figure 3 shows comparisons between the experimental data for the $42D_{5/2}$ state and the simulations by a mean-field model (see Supplementary information), where we use an interaction $U(r) = -C_k/r^k$ which is a dipole-dipole interaction ($k = 3$) at short interatomic distances that changes into a van der Waals interaction ($k = 6$) at long

interatomic distances in Eq. (3). The coefficient C_3 of the dipole-dipole interaction and the crossover radius r_c where k changes from 3 to 6 serve as adjusting parameters. The continuity of the interaction potential U as a function of r defines the van der Waals coefficient by $C_6 = C_3 r_c^3$. Figures 3a and b show that reasonable agreements can be found for the Ramsey contrast between the measurements and the mean-field simulations, which are the results of averaging over an inhomogeneous atom distribution in the trap (see Supplementary Information) with $C_3 = 3.4 \text{ GHz}\mu\text{m}^3$ and $r_c = 0.81 \mu\text{m}$. These values for C_3 and r_c yield the phase-shifts simulated by the mean-field model in Figs. 3c and d. Here the zero-delay offset of the simulated phase shift is arbitrary and set to 0 degree. It is seen in these figures that the mean-field simulation gives a phase-shift whose amount of change as a function of τ is larger than the measured one by

more than an order of magnitude, thereby clearly failing to reproduce our observations. This discrepancy between measured and simulated phase-shifts is not improved by introducing anisotropic interactions (see Supplementary Information).

We find that a qualitative improvement over the mean-field results can be obtained by analytical derivation of $P(\tau)$ for the many-body interacting system (see Supplementary Information). This allows us to derive a method to efficiently describe the dynamics for any strength of interactions. This is somewhat similar to the methods presented in Refs. 34 and 35 and is hereafter referred to as ‘‘analytic Ramsey model (ARM)’’. For any given atom j interacting with $N - 1$ neighboring Rydberg atoms we derive

$$P_j(\tau) = 2p_g p_e \left\{ 1 + \sum_{\ell=1}^N p_g^{(N-\ell)} p_e^{\ell-1} \times \sum_{\substack{\text{card}(I)=\ell-1 \\ I \subset \{1, \dots, N\} \setminus \{j\}}} \cos \left[\left(\omega + \sum_{k \in I} \Delta_{jk} \right) \tau + \phi \right] \right\}, \quad (4)$$

where $\text{card}(I)$ is the cardinality of the set I , $p_g = c_g c_g^*$ and $p_e = c_e c_e^*$ are the ground- and Rydberg-state populations produced by the initial pump excitation, respectively, and $\Delta_{ij} = U(r_{ij})/\hbar$ describes a frequency-shift induced by the interaction between atoms i and j . Setting $\Delta_{ij} = 0$ reduces Eq. (4) to the standard Ramsey signal $P_j(\tau) = 2p_g p_e (1 + \cos[\omega\tau + \phi])$, which is similar to Eq. (1), with $\omega = (E_e - E_g)/\hbar$ being the atomic-resonance frequency, and ϕ is the phase offset arising from AC-Stark shifts during the ps pulse excitations (see Supplementary Information).

Equation (4) represents an exact solution for the dynamics described by a Hamiltonian of the form presented in Eq. (3). However, it still involves costly computational effort. Further analytical progress is possible by using a continuum approximation for the density distribution of Rydberg atoms $n(\mathbf{r})$. We then assume that for each position \mathbf{r} the density n is constant within a sphere of radius r_0 , which is a tunable cutoff parameter. Neglecting all the interaction terms $U(\mathbf{r})$ with $|\mathbf{r}| > r_0$ and $|\mathbf{r}| < r_B$, where r_B is the blockade radius due to the finite bandwidth of the excitation with the IR and blue pulses, allows us to replace N by the number of atoms $N_0(\mathbf{r}) = 4\pi n(\mathbf{r})(r_0^3 - r_B^3)/3$ within this shell in Eq. (4). This leads to the following expression for the τ -dependent signal

$$P(\tau) = 2p_g p_e \{ 1 + |g(\tau)| \cos(\omega\tau + \alpha(\tau) + \phi) \}, \quad (5)$$

where $P(\tau) = \int_V d\mathbf{r} n(\mathbf{r}) P(\mathbf{r}, \tau)/N$, V is the volume of the atomic ensemble, and $P(\mathbf{r}, \tau)$ is the continuous Rydberg population density (see Supplementary information). The contrast-decay $|g(\tau)|$ and phase-shift $\alpha(\tau)$ are obtained from $g(\tau) \equiv |g(\tau)|e^{i\alpha(\tau)}$, which for the case of

isotropic interactions reduces to the simple expression

$$g(\tau) = \frac{4\pi}{N} \int_0^\infty dr r^2 n(r) \times \left[p_g + p_e \frac{3}{r_0^3 - r_B^3} \int_{r_B}^{r_0} ds s^2 e^{iU(s)\tau/\hbar} \right]^{N_0(r)-1}. \quad (6)$$

For a non-interacting system Eq. (6) reduces to the independent atom result with $g(\tau) = 1$ as $p_g + p_e = 1$. For an interacting system Eq. (6) can be numerically evaluated easily for essentially arbitrary large values of N_0 , in contrast to Eq. (4).

Figure 4 shows comparisons between the experimental data for the $42D_{5/2}$ state and the simulations by ARM with Eq. (5), where we consider an interaction $U(r)$ to be a dipole-dipole interaction at short interatomic distances and a van der Waals interaction at long interatomic distances. The coefficient C_3 of the dipole-dipole interaction, the crossover radius r_c , and the zero-delay offset of the phase-shift serve as adjusting parameters. The adjustment includes an averaging over the density distribution in the dipole trap. The solid lines in Fig. 4 represent the simulations with the parameters $C_3 = 4.3 \text{ GHz } \mu\text{m}^3$ and $r_c = 1.95 \mu\text{m}$ and agree reasonably with the measured Ramsey contrasts and phase-shifts for both of the Rydberg populations $p_e \sim 1.2\%$ and 3.3% used in the measurement. Figure 5 shows the simulated values for the Ramsey contrast and phase-shift at $\tau = 500$ ps with the population of the $42D_{5/2}$ being $\sim 3.3\%$ as functions of a cutoff radius r_0 at which we truncate the integration in Eq. (6). It is seen in this figure that the simulated Ramsey contrast and phase-shift almost converge for r_0 larger than $4 \mu\text{m}$, where their amounts of change reach more than 90 percent of the ones at $r_0 = 6 \mu\text{m}$, and those converged values agree well with the measured ones indicated by the dark-gray solid lines, each of which is the average over the eight points around $\tau = 500$ ps in Fig. 4b or d. This $r_0 \sim 4 \mu\text{m}$ gives the average atom number within the volume $V = \frac{4\pi}{3}(r_0^3 - r_B^3)$ to be ~ 120 , demonstrating that the interaction of several tens to a hundred of atoms are necessary to reproduce our observations.

By taking the limit for large atom number N_0 in Eq. (6) a decay constant can be obtained for the Ramsey-contrast reduction. For $p_e \sim 3.3\%$ and $C_6 = C_3 r_c^3$ derived from the simulation of the Ramsey contrast presented in Fig. 4, the decay constant is approximately given by $\sigma = p_e \frac{\pi}{3} \sqrt{\frac{8\pi C_6}{\hbar}} n_{av} \sim 3.5 \times 10^4 \text{ (Hz)}^{1/2}$, where $n_{av} = \frac{1}{2^{3/2}} n_p$ (n_p being the peak density) is the density averaged over the whole ensemble (see Supplementary Information). The pump-probe delay to reach $e^{-1} (\sim 0.37)$ of the initial contrast is given by $1/\sigma^2 \sim 810$ ps, which agrees well with our measurement time of 500 ps giving the reduction to 45%.

We find that the $C_3 = 4.3 \text{ GHz } \mu\text{m}^3$ used for the simulation is comparable to the value 1.7 GHz extrapolated from the C_3 measured at longer interatomic distances for

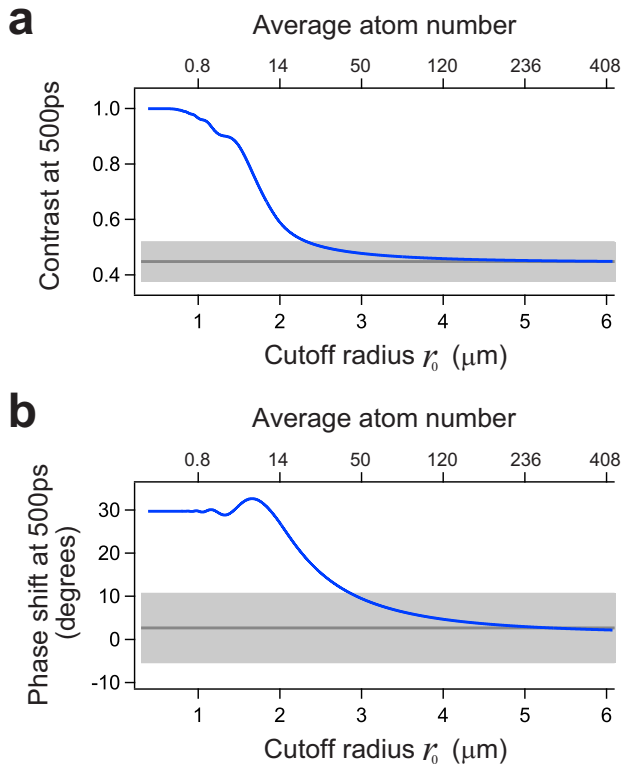


FIG. 5: **Convergence of the Ramsey contrast and phase-shift simulated by ARM as functions of the cutoff radius r_0 .** The Ramsey contrast and the phase-shift at $\tau = 500$ ps simulated by ARM with the population of the $42\text{D}_{5/2}$ being $\sim 3.3\%$ are plotted as functions of the cutoff radius r_0 (the lower abscissa) and the average atom number within the volume $V = \frac{4\pi}{3}(r_0^3 - r_B^3)$ (the higher abscissa). The interaction strength in these simulations is limited below 75 GHz, which is the half width half maximum of the pump excitation, and the peak atom density is set to $\sim 1.3 \times 10^{12} \text{ cm}^{-3}$ in these simulations. The simulated Ramsey contrast and phase-shift almost converge for r_0 larger than $4 \mu\text{m}$, where their amounts of change reach more than 90 percent with respect to those at $r_0 = 6 \mu\text{m}$. The converged values agree well with the measured ones indicated by the dark-gray solid lines, each of which is the average over eight points around 500 ps in Fig. 4b or d. The light-gray shaded area represents one standard deviation of the average over the eight measured values. This convergence around $4 \mu\text{m}$ demonstrates that the interaction of several tens to a hundred of atoms are necessary to reproduce our observations. In contrast to the mean field model the ARM gives a minimum number of interacting atoms for a given evolution time.

the two-body interaction of $\nu = 62$ (Ref. 25), assuming an ν^4 dependence of the C_3 value. The combination of the $C_3 = 4.3 \text{ GHz } \mu\text{m}^3$ and $r_c = 1.95 \mu\text{m}$ used for the simulation gives $C_6 = 32 \text{ GHz } \mu\text{m}^6$, which is one order larger than the value for C_6 extrapolated from the one measured at longer interatomic distances for the two-body interaction in Ref. 36. This discrepancy in the

C_6 value might result from the difference between the two-atom and many-atom potentials. It might also arise from the current effective treatment of the interaction (see Supplementary Information). The half-width-half-maximum bandwidth of the present Rydberg excitation with the ps IR and blue pulses is around 75 GHz, giving a blockade radius of $r_B \sim 0.39 \mu\text{m}$ for the obtained C_3 -coefficient. According to Fig. 1d, this blockade radius is shorter than the average nearest-neighbor distance and the corresponding volume encompasses only ~ 0.3 atoms at the peak density in the atomic ensemble, thereby the effects of the interaction blockade are largely negligible.

We have also performed other series of ARM simulations with a pure dipole-dipole or van der Waals interaction as well as with an anisotropic potential. Details of these simulations are given in Supplementary Information.

The crossover radius $r_c = 1.95 \mu\text{m}$ used for the simulations in Fig. 4 gives $N_0 \sim 40$ atoms located within the sphere given by this radius at the peak density in the atomic ensemble. Those ~ 40 atoms are strongly connected by the dipole-dipole interaction, whereas the other atoms outside the sphere are coupled by the van der Waals interaction, which decays quickly as the radius becomes larger. By inspection of the actual adiabatic interaction potentials between two Rydberg atoms (see Supplementary Information), we find that this value $r_c = 1.95 \mu\text{m}$ also matches the largest length scale where the dipole-dipole interaction is dominant over the van der Waals interaction. We note that for shorter distances $r \ll r_c$ the bandwidth of our Rydberg excitation with the ps IR and blue pulses covers multiple adiabatic interactions-potentials that can hybridize with the one correlating asymptotically to the $42\text{D} + 42\text{D}$ limit. While in principle this could affect the contrast decay, the present model based on a single effective potential captures the observed dynamics both for the Ramsey contrast and the phase-shift.

It is seen clearly in Figs. 3 and 4 that the dephasing is accelerated when the Rydberg population is increased from $\sim 1.2\%$ to $\sim 3.3\%$. Figure 6 shows Ramsey contrasts as functions of τ for three different Rydberg levels $\nu = 38, 42,$ and 50 . The populations p_e and estimated peak atom-densities are $p_e \sim 3.2\%$ and $\sim 1.2 \times 10^{12} \text{ cm}^{-3}$ for $\nu = 38$, $p_e \sim 3.3\%$ and $\sim 1.3 \times 10^{12} \text{ cm}^{-3}$ for $\nu = 42$, and $p_e \sim 3.1\%$ and $\sim 1.2 \times 10^{12} \text{ cm}^{-3}$ for $\nu = 50$, respectively (see Methods for these density estimations). It is seen from this Figure that the dephasing is accelerated also by increasing the principal quantum number ν of the Rydberg level. These results demonstrate that the ultrafast many-body dynamics can be actively controlled by tuning the population and the principal number of the Rydberg level. It should be noted that several Rydberg states are excited in the case of $\nu=50$ in Fig. 6 (see Supplementary Information), but we nevertheless simplify our treatment to the single excited Rydberg state case,

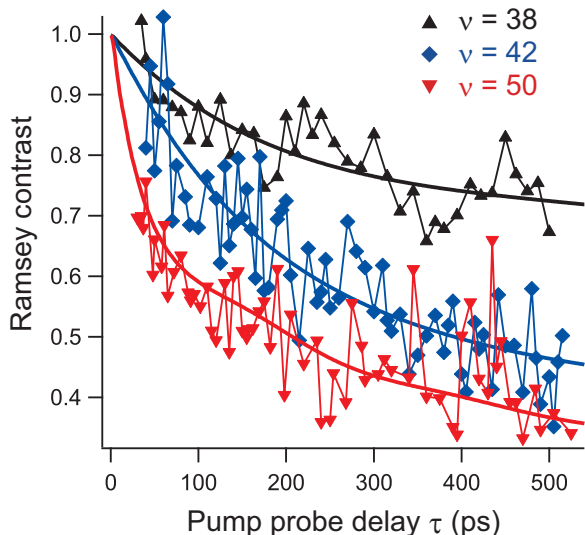


FIG. 6: **Active control of the ultrafast many-body electron dynamics.** Measured Ramsey contrasts are plotted as functions of τ for three different Rydberg levels $\nu = 38$, 42, and 50. The populations p_e and estimated peak atom-densities are $p_e \sim 3.2\%$ and $\sim 1.2 \times 10^{12} \text{ cm}^{-3}$ for $\nu = 38$, $p_e \sim 3.3\%$ and $\sim 1.3 \times 10^{12} \text{ cm}^{-3}$ for $\nu = 42$, and $p_e \sim 3.1\%$ and $\sim 1.2 \times 10^{12} \text{ cm}^{-3}$ for $\nu = 50$, respectively (see Methods for these density estimations). The ARM simulations indicated by the black, blue, and red solid-lines yield adjusting parameters to be $C_3 = 2.7 \text{ GHz } \mu\text{m}^3$ and $C_6 = 7 \text{ GHz } \mu\text{m}^6$ for $\nu = 38$, $C_3 = 4.3 \text{ GHz } \mu\text{m}^3$ and $C_6 = 32 \text{ GHz } \mu\text{m}^6$ for $\nu = 42$, and $C_3 = 20 \text{ GHz } \mu\text{m}^3$ and $C_6 = 100 \text{ GHz } \mu\text{m}^6$ for $\nu = 50$. The interaction strength in these simulations is limited below 75 GHz, which is the half width half maximum of the pump excitation, and the peak atom-density is set to the estimated density for each Rydberg level in these simulations. It should be noted that several Rydberg states are excited in the case of $\nu=50$ (see Supplementary Information). However, we consider an excitation to a single Rydberg state to perform the simulations for all of the three Rydberg levels.

in which the ARM simulations give a good agreement to experimental results as witnessed by the solid lines in Fig. 6. We have also measured the dependence of the Ramsey-contrast decay on the atom density, which could naturally be another useful tuning knob of the many-body dynamics (see Supplementary Information for this atom-density dependence).

The theoretical analysis developed here could in principle be extended to investigate beyond-mean-field effects in Ramsey experiments with more complex Hamiltonians, such as Heisenberg-type Hamiltonians of interest for polar molecules [6] and atomic clocks [37] in optical lattices. Experiments similar to the ones demonstrated here could be implemented in thermal cells at room temperature [38] if one can compensate the relevant Doppler shift, which is comparable to the interaction-induced phase-shift.

Our Rydberg gas is a disordered ensemble of strongly-correlated particles and may have similarities with other disordered many-body systems including liquids. It is well known that molecular properties such as chemical reactivities are modified in liquids with respect to those observed in the gas phase. Such modification arises from a many-body interaction among solute and solvent molecules, which has often been interpreted in terms of the mean-field model [39]. This mean field interpretation could be justified as long as one considers an equilibrium property that appears as a consequence of many collisions. It is an interesting question, however, whether the mean-field model applies also to electron dynamics, which could proceed on timescales shorter than average collision times in liquids and is believed to determine the subsequent rearrangement of molecular bonds in chemical reactions [40]. Our present observation demonstrates that the motion of the electronic wave-packet is modulated by many-body interactions beyond mean-field, suggesting that many-body correlations may also have an important influence on the electron dynamics in liquids. Our approach thus opens a new avenue to observe and manipulate nonequilibrium dynamics of strongly interacting many-body systems on the ultrafast timescale.

-
- [1] Bloch, I., Dalibard, J. & Zwerger, W. Many-body physics with ultracold gases. *Rev. Mod. Phys.* **80**, 885–964 (2008).
 - [2] Lahaye, T., Menotti, C., Santos, L., Lewenstein, M. & Pfau, T. The physics of dipolar bosonic quantum gases. *Rep. Prog. Phys.* **72**, 126401 (2009).
 - [3] Baranov, M. A., Dalmonte, M., Pupillo, G. & Zoller, P. Condensed matter theory of dipolar quantum gases. *Chem. Rev.* **112**, 5012–5061 (2012).
 - [4] Richerme, P. *et al.* Non-local propagation of correlations in quantum systems with long-range interactions. *Nature* **511**, 198–201 (2014).
 - [5] Jurcevic, P. *et al.* Quasiparticle engineering and entanglement propagation in a quantum many-body system. *Nature* **511**, 202–205 (2014).
 - [6] Yan, B. *et al.* Observation of dipolar spin-exchange interactions with lattice-confined polar molecules. *Nature* **501**, 521–525 (2013).
 - [7] Takekoshi, T. *et al.* Ultracold dense samples of dipolar RbCs molecules in the rovibrational and hyperfine ground state. *Phys. Rev. Lett.* **113**, 205301 (2014).
 - [8] Saffman, M., Walker, T. G. & Mølmer, K. Quantum information with Rydberg atoms. *Rev. Mod. Phys.* **82**, 2313–2363 (2010).
 - [9] Comparat, D. & Pillet, P. Dipole blockade in a cold Rydberg atomic sample. *J. Opt. Soc. Am. B* **27**, A208–A232 (2010).
 - [10] Tong, D. *et al.* Local blockade of Rydberg excitation in an ultracold gas. *Phys. Rev. Lett.* **93**, 063001 (2004).
 - [11] Gallagher, T. F. *Rydberg Atoms* (Cambridge Univ. Press, 1994).
 - [12] Wyker, B. *et al.* Creating and transporting Trojan wave

- packets. *Phys. Rev. Lett.* **108**, 043001 (2012).
- [13] Jaksch, D. *et al.* Fast quantum gates for neutral atoms. *Phys. Rev. Lett.* **85**, 2208–2211 (2000).
- [14] Lukin, M. *et al.* Dipole blockade and quantum information processing in mesoscopic atomic ensembles. *Phys. Rev. Lett.* **87**, 037901 (2001).
- [15] Dudin, Y. O. & Kuzmich, A. Strongly interacting Rydberg excitations of a cold atomic gas. *Science* **336**, 887–889 (2012).
- [16] Firstenberg, O. *et al.* Attractive photons in a quantum nonlinear medium. *Nature* **502**, 71–75 (2013).
- [17] Baur, S., Tiarks, D., Rempe, G. & Dürr, S. Single-photon switch based on Rydberg blockade. *Phys. Rev. Lett.* **112**, 073901 (2014).
- [18] Weimer, H., Müller, M., Lesanovsky, I., Zoller, P. & Büchler, H. P. A Rydberg quantum simulator. *Nature Phys.* **6**, 382–388 (2010).
- [19] Schauß, P. *et al.* Observation of spatially ordered structures in a two-dimensional Rydberg gas. *Nature* **491**, 87–91 (2012).
- [20] Viteau, M. *et al.* Rydberg excitations in Bose-Einstein condensates in quasi-one-dimensional potentials and optical lattices. *Phys. Rev. Lett.* **107**, 060402 (2011).
- [21] Schempp, H. *et al.* Full counting statistics of laser excited Rydberg aggregates in a one-dimensional geometry. *Phys. Rev. Lett.* **112**, 013002 (2014).
- [22] Nipper, J. *et al.* Highly resolved measurements of Stark-tuned Förster resonances between Rydberg Atoms. *Phys. Rev. Lett.* **108**, 113001 (2012).
- [23] Nipper, J. *et al.* Atomic pair-state interferometer: controlling and measuring an interaction-induced phase shift in Rydberg-atom pairs. *Phys. Rev. X* **2**, 031011 (2012).
- [24] Bettelli, S. *et al.* Exciton dynamics in emergent Rydberg lattices. *Phys. Rev. A* **88**, 043436 (2013).
- [25] Barredo, D. *et al.* Coherent excitation transfer in a spin chain of three Rydberg atoms. *Phys. Rev. Lett.* **114**, 113002 (2015).
- [26] Ohmori, K. Wave-packet and coherent control dynamics. *Annu. Rev. Phys. Chem.* **60**, 487–511 (2009).
- [27] Alber, G. & Zoller, P. Laser excitation of electronic wave packets in Rydberg atoms. *Phys. Rep.* **199**, 231–280 (1991).
- [28] Zhou, T., Li, S. & Jones, R. R. Rydberg-wave-packet evolution in a frozen gas of dipole-dipole-coupled atoms. *Phys. Rev. A* **89**, 063413 (2014).
- [29] Anderson, W. R., Veale, J. R. & Gallagher, T. F. Resonant dipole-dipole energy transfer in a nearly frozen Rydberg gas. *Phys. Rev. Lett.* **80**, 249–252 (1998).
- [30] Mourachko, I. *et al.* Many-body effects in a frozen Rydberg gas. *Phys. Rev. Lett.* **80**, 253–256 (1998).
- [31] Kutteruf, M. R. & Jones, R. R. Probing electronic coherence in a gas of dipole-dipole coupled Rydberg atoms. *Phys. Rev. Lett.* **108**, 013001 (2012).
- [32] Tanner, P. J., Han, J., Shuman, E. S. & Gallagher, T. F. Many-body ionization in a frozen Rydberg gas. *Phys. Rev. Lett.* **100**, 043002 (2008).
- [33] Katsuki, H., Kayanuma, Y. & Ohmori, K. Optically engineered quantum interference of delocalized wave functions in a bulk solid: the example of solid *para*-hydrogen. *Phys. Rev. B* **88**, 014507 (2013).
- [34] Rey, A. M. *et al.* Probing many-body interactions in an optical lattice clock. *Ann. Phys.* **340**, 311–351 (2014).
- [35] Maze, J. R., Taylor, J. M. & Lukin, M. D. Electron spin decoherence of single nitrogen-vacancy defects in diamond. *Phys. Rev. B* **78**, 094303 (2008).
- [36] Béguin, L., Vernier, A., Chicireanu, R., Lahaye, T. & Browaeys, A. Direct measurement of the van der Waals interaction between two Rydberg atoms. *Phys. Rev. Lett.* **110**, 263201 (2013).
- [37] Martin, M. J. *et al.* A quantum many-body spin system in an optical lattice clock. *Science* **341**, 632–636 (2013).
- [38] Baluktian, T., Huber, B., Löw, R. & Pfau, T. Evidence for strong van der Waals type Rydberg-Rydberg interaction in a thermal vapor. *Phys. Rev. Lett.* **110**, 123001 (2013).
- [39] Friedman, H. L. *A Course in Statistical Mechanics* (Prentice-Hall, 1985).
- [40] Jimenez, R., Fleming, G. R., Kumar, P. V. & Maroncelli, M. Femtosecond solvation dynamics of water. *Nature* **369**, 471–473 (1994).

Acknowledgements We thank T. Pfau, R. Löw, D. Jaksch, M. Kiffner, A. Browaeys, T. Lahaye, V. Vuletić, I. Lesanovsky, R. J. Levis, R. J. D. Miller, I. Ohmine, S. Saito, and T. Yanai for fruitful discussions. This work was partly supported by Grant-in-Aid for Scientific Research by JSPS, Photon Consortium by MEXT. C.G. was supported from the Austrian Science Fund (FWF) via project P24968-N27. G.P. was supported by ERC-St Grant ColdSIM (No. 307688), EOARD, RySQ, UdS via IdEX and ANR via BLUESHIELD. K.O. thanks Alexander von Humboldt foundation, University of Heidelberg, and University of Strasbourg for supporting this international collaboration.

METHODS

Atom preparation. A magneto-optical trap (MOT) of ^{87}Rb atoms was loaded from background vapor for 1.4 s. During the subsequent MOT compression for 30 ms, an optical dipole trap was turned on. The dipole trap was composed of a single 1064 nm beam with its power and beam-waist being ~ 4 W and ~ 30 μm ($1/e^2$ radius), respectively. Polarization gradient cooling was performed for 100 ms. The trapped atoms were then transferred into the $F = 1$ ground state by switching off the MOT repump laser. After that, we turned off the MOT trapping beams and the magnetic field. While keeping the intensity of the dipole trap laser, plain evaporative cooling was carried out for 50 ms. During the evaporation process, a 76 μT homogeneous magnetic field was turned on, pointing along the direction of the dipole trap laser. For the next 200 μs , the atoms were optically pumped to the $|5S_{1/2}, F = 2, m_F = +2\rangle$ state by using the MOT repump beam and a σ^+ beam which is resonant to the transition from $|5S_{1/2}, F = 2\rangle$ to $|5P_{3/2}, F' = 2\rangle$ and counterpropagates with the dipole trap laser. The dipole-trap laser is turned off 2 μs before the irradiation of the ps IR and blue pulses to avoid 2+1 multiphoton ionization induced by a combination of the ps pulses and the trapping laser beam, whereas the homogeneous magnetic field remained

on. The ps IR and blue pulses at ~ 779 nm and ~ 481 nm, which propagated collinearly with the dipole trap beam, had cross-sections with FWHMs of about 130 (100) μm and 30 (30) μm along the x (y) direction (Fig. 1a).

Estimation of the atom density. At first the atom density in the Ramsey measurements was estimated solely from the total number of atoms and the size of the atomic ensemble obtained by in-situ absorption imaging with a CCD camera without expanding the atomic ensemble. In contrast to the axial size of the atomic ensemble (~ 2 mm FWHM), however, the spatial resolution of the in-situ absorption imaging with the CCD camera (8.3 μm) was not high enough to resolve the radial size, resulting in an underestimation of the atom density.

In a later independent experiment, hereafter referred to as a “reference experiment”, we estimated the radial size from the temperature of the atomic ensemble and the trap frequency of the radial direction, setting the trapping conditions almost the same as those employed in the Ramsey measurements. Those trapping conditions set almost the same are (1) the same loading sequence as described in the preceding subsection; (2) the dipole-trap laser power (with an error described in the next sentence); (3) the dipole-trap laser focusing; and (4) the total number of atoms (with an error described in the next sentence). We performed two reference experiments under two different trapping conditions corresponding to the higher and lower densities described in the main text, setting the dipole-trap laser power (the trapping condition (2)) with a difference of $\sim 2\%$ and $\sim 5\%$ from the power averaged over the Ramsey measurements for the higher and lower densities, respectively, and setting the total number of atoms (the trapping condition (4)) within one standard deviations $\sim 14\%$ and $\sim 33\%$ of the eight and seven corresponding values measured in the Ramsey measurements for the higher and lower densities, respectively. In these reference measurements, the temperature was measured by an expansion of the atomic ensemble, and parametric heating was employed to infer the radial trap frequency. The temperatures and the trap frequencies were thus obtained to be ~ 67 $\mu\text{K} / 2.2$ kHz and ~ 39 $\mu\text{K} / 1.1$ kHz under those two trapping conditions, respectively. These temperatures and trap frequencies give typical radial sizes (FWHM) of the atomic ensembles in the reference experiments to be about 14 μm and 20 μm , which we regarded to be the radial sizes of the atomic ensembles in the Ramsey measurements for the higher and lower densities, respectively.

The total number of atoms was also slightly underestimated by the in-situ absorption imaging in the Ramsey measurements because of the spatial resolution of the CCD camera, so that it was calibrated in a later independent experiment in which the loading sequence and the trap laser focusing (the trapping conditions (1) and (3)) were almost the same as those employed in the Ramsey measurements. In this calibration experiment, we

measured the total number of atoms by the absorption imaging with the expansion of the atomic ensemble as a function of the one measured without the expansion to obtain a linear calibration curve with its slope being 1.04 ± 0.03 . This linear calibration curve gives the total numbers of atoms to be $\sim 6 \times 10^5$ and $\sim 4 \times 10^4$ for the higher and lower densities described in the main text, respectively, for $\nu = 42$.

These radial sizes and the total numbers of atoms are combined with the axial sizes measured in-situ in the Ramsey measurements to give the peak atom-densities of $\sim 1.3 \times 10^{12}$ cm^{-3} and $\sim 4 \times 10^{10}$ cm^{-3} for the higher and lower densities described in the main text, respectively, for $\nu = 42$. Similarly the peak atom-density and the total number of atoms for $\nu = 38$ are estimated to be $\sim 1.2 \times 10^{12}$ cm^{-3} and $\sim 5 \times 10^5$ for the higher density and $\sim 4 \times 10^{10}$ cm^{-3} and $\sim 4 \times 10^4$ for the lower density, respectively, and for $\nu = 50$ they are estimated to be $\sim 1.2 \times 10^{12}$ cm^{-3} and $\sim 4 \times 10^5$ for the higher density and $\sim 3 \times 10^{10}$ cm^{-3} and $\sim 3 \times 10^4$ for the lower density, respectively.

Estimation of the temperature. The temperature of the atomic ensemble was not measured in situ in a series of the Ramsey measurements, but it was measured in a later independent experiment, hereafter referred to as a “temperature experiment”, in which we set the trapping conditions (1)(4) in the same way as described in the preceding subsection. In this temperature experiment, the temperature was measured by an expansion of the atomic ensemble. Two temperature experiments were performed independently under the trapping conditions corresponding to the higher density described in the main text, giving ~ 67 μK and ~ 72 μK , respectively, so that we estimated the temperature of the higher density ensemble to be ~ 70 μK in the Ramsey measurements. Similarly a temperature experiment was performed independently under the trapping conditions corresponding to the lower density described in the main text, giving ~ 39 μK , so that we estimated the temperature of the lower density ensemble to be ~ 39 μK in the Ramsey measurements.

Rydberg excitation and detection. The output of a Ti:sapphire laser system (Spectra Physics; Spitfire Ace, wavelength ~ 779 nm, pulse width ~ 1 ps, repetition rate 1 kHz) was used as the IR pulse and was also used to pump an optical parametric amplifier (Spectra Physics; TOPAS) to generate the blue pulse tuned to ~ 481 nm. The repetition rate was reduced using pulse pickers to synchronize it with the atom preparation sequence whose duration was 1.6 s. In order to reduce the number of Rydberg states to be excited, the spectra of those IR and blue pulses were cut to be about 0.13 nm and 0.20 nm, respectively, using homemade pulse shapers in a 4f-setup ($f = 500$ mm), respectively. The IR and blue pulses were combined collinearly with a dichroic mirror, and their relative timing was coarsely adjusted to be zero by cross-

correlation measurements based on sum-frequency generation and was further optimized to maximize the Rydberg ion signals. They were introduced into a Michelson-type interferometer to produce a pair of identical double-pulses, each of which is composed of the IR and blue pulses. Those two double-pulses induce the pump and probe excitations, respectively (see Fig. 1a). The relative phase between these two double-pulses were tuned with attosecond precision [33]. Those two double-pulses were combined collinearly with the dipole-trap laser-beam with another dichroic mirror. Those two double-pulses and the trapping laser beam were focused with a plano-convex lens ($f = 250$ mm) to the atomic ensemble.

The IR and blue pulses and the optical pumping beam are circularly polarized in the same direction with respect to the magnetic field, so that the state $\nu D_{5/2, m_J = +5/2}$ was mostly populated, and excitations to S Rydberg states were suppressed due to transition selection-rules even though the effective two-photon excitation spectrum covered the S states. This excitation scheme also suppressed the Raman transition between the F=2 and F=1 hyperfine states in the ground state that could happen within the single IR pulse to induce undesirable beating in the Ramsey contrast as a function of τ , an example of which is shown in Fig. 2d, with a period of 146 ps, which is the reciprocal of the hyperfine splitting 6.83 GHz.

The maximum population of the νD Rydberg states was not larger than 5% in order to suppress photo-ionization. The typical pulse energies of the IR and blue pulses were about 10 and 400 nJ, respectively, for the 1.2% population and were about 30 and 600 nJ, respectively, for the 3.3% population. The population was estimated from the loss of the number of the ground state atoms induced by the irradiation of the ps IR and blue pulses. We measured the number of the atoms by absorption imaging with and without the ps pulses and compared those numbers to evaluate the loss. See the previous subsection ‘‘Estimation of the atom density’’ for the details of the evaluation of the atom number by absorption imaging. The loss induced by a single pair of the IR and blue pulses was too small (a few percent) to be evaluated securely, so that we shined 30 or 50 pairs of the IR and blue pulses, each of which was accompanied by field ionization [11], at a 1 kHz repetition rate to induce the loss that was clearly visible and was used to infer the loss induced by the single pair of the IR and blue pulses. The loss for different amounts of pulse pairs followed the relation $(\frac{N_r}{N_t}) = (1 - p_e)^q$, where N_r is the number of atoms remaining after q pulses and N_t is the total atom number. p_e is the Rydberg state population for the atoms in the ensemble.

After the probe excitation, the populated Rydberg states were ionized by means of field ionization. The Rb^+ ions thus produced were detected with a micro channel plate (MCP) placed 5.5 cm away from the atomic ensemble. The electric field for the ionization was triggered

50 ns after the probe excitation, reaching the ionization threshold within the next 100 ns. The output of the MCP was amplified with a preamplifier and sent to a gated integrator, whose output was fed into a computer. Note that the field-ionization spectrum shown in Fig. 1c was measured using an oscilloscope with the electric field ramped up slowly on the microsecond timescale to check how many Rydberg states were populated by our broadband excitation with the ps pulses.

Time-domain Ramsey interferometry. The interaction among Rydberg atoms was observed by time-domain Ramsey interferometry with a pair of two-photon excitations: pump and probe. Their delay τ was coarsely tuned on the picosecond timescale with a motorized mechanical stage placed in one arm of the interferometer mentioned above and was scanned finely on the attosecond timescale with a piezoelectric transducer to measure Ramsey interferograms. A He-Ne laser beam was introduced to the interferometer to check the linearity of the scan by monitoring its optical interference. The period of this optical interference was also used for the calibration of the pump-probe delay τ . We measured the field-ionization signals of the two atomic ensembles with different densities alternately to suppress systematic uncertainties, scanning τ in steps of ~ 30 attoseconds over a range of ~ 3 fs at each coarse delay tuned by the mechanical stage on the picosecond timescale. The obtained Ramsey interferogram was fitted with a sinusoidal function. As the expected energy shift induced by the interaction was at most on the order of 10 GHz, much smaller than the eigenfrequency of the Rydberg state itself ($\sim 1 \times 10^{15}$ Hz), we fitted the interferograms with the same eigenfrequencies for the higher- and lower-densities to evaluate the phase-shift of the higher-density ensemble from the lower-density one. We have defined the contrast of the interferogram to be the ratio of the amplitude of the fitted sinusoidal function to its mean value. In Figs. 2a, b and c, the signal intensities are normalized by the mean value of the sinusoidal function fitted to each interferogram. We have defined Ramsey contrast to be the ratio of the contrast of the higher-density ensemble to that of the lower-density one, as shown in Figs. 3, 4, 5 and 6. We assume that many-body interactions are negligible in the lower-density ensemble, which is thus taken to be a reference for measuring the contrast decay and the phase-shift that may be induced by the interactions in the higher-density ensemble.

Supplementary Information

TIME-DOMAIN VERSUS FREQUENCY-DOMAIN RAMSEY INTERFEROMETRY

We consider a one-photon excitation of a two-level system with rectangular laser pulses for simplicity. A pulse sequence in Ramsey interferometry is schematically illustrated in Supp. Fig. 1. The pump and probe laser pulses $\mathbf{E}(t)$ and $\mathbf{E}(t-\tau)$ in the time-domain Ramsey interferometry are produced with a beam splitter in the optical interferometer, duplicated from one common laser pulse, so that they have the same carrier envelope phases (CEPs), as is depicted by the black solid lines in Supp. Fig. 1. The Ramsey oscillation is measured as a function of the time delay τ between those two identical pulses. In the frequency-domain Ramsey interferometry, however, the pump and probe pulses are often cut out from one common CW laser field by amplitude modulation, so that the CEP of the probe pulse is given by the blue solid line in Supp. Fig. 1. The Ramsey oscillation is then measured as a function of the laser detuning from the resonance frequency of the two-level system. One advantage of the time-domain Ramsey interferometry is that it gives a Ramsey oscillation identical to the temporal oscillation of the upper state wave-function of the two-level system except that the real time t is replaced by the pump-probe delay τ . Therefore one can directly measure the temporal oscillation of the upper-state wave-function by scanning τ .

DISCUSSION ON THE ZERO-DELAY OFFSET IN THE PHASE-SHIFT

We consider a one-photon excitation of a two-level system with rectangular ps laser pulses for simplicity. The results can be easily adapted to near-resonant two-photon excitations that have been used in the present experiments.

Solving the time dependent Schrödinger equation, we obtain the same expression for the pump and probe pulses, $\mathbf{E}(t)$ and $\mathbf{E}(t-\tau)$, given by

$$A = \begin{pmatrix} (\cos(\theta/2) - i\eta \sin(\theta/2))e^{i\frac{\omega_l}{2}\delta t} & -i\xi \sin(\theta/2)e^{i\chi}e^{i\frac{\omega_l}{2}\delta t} \\ -i\xi \sin(\theta/2)e^{-i\chi}e^{-i\frac{\omega_l}{2}\delta t} & (\cos(\theta/2) + i\eta \sin(\theta/2))e^{-i\frac{\omega_l}{2}\delta t} \end{pmatrix} = \begin{pmatrix} c_g & ic_e \\ ic_e^* & c_g \end{pmatrix} \quad (S1)$$

with $\theta = \Omega\delta t$, $\eta = \Delta/\Omega$, $\xi = \Omega_R/\Omega$, and $\Omega = \sqrt{\Omega_R^2 + \Delta^2}$, where Ω_R is the Rabi frequency, and $\Delta = \omega - \omega_l$ is the detuning of the laser frequency ω_l from the atomic resonance ω . The time δt is the duration of the ps pulse, and χ represents the phase of the complex Rabi frequency $\tilde{\Omega}_R = \Omega_R e^{i\chi}$. The amplitudes c_g and c_e are complex numbers. The pump excitation is given by this matrix A operated on the ground state defined by a column matrix $(1 \ 0)^T$. Note that the matrix $(0 \ 1)^T$ describes 100% population in the upper state.

The matrix for the excitation can be expressed in the form

$$A = \begin{pmatrix} |c_g|e^{i\phi/2} & i|c_e|e^{i\zeta/2} \\ i|c_e|e^{-i\zeta/2} & |c_g|e^{-i\phi/2} \end{pmatrix}, \quad (S2)$$

where $|c_g|^2 + |c_e|^2 = 1$ and ϕ and ζ are phases of the complex amplitudes c_g and c_e , respectively. Here only the phase ϕ remains in the Ramsey signal, while the phase ζ is cancelled out (see the main text). The phase ϕ is defined by

$$\tan(\phi/2) = \frac{\Omega \sin(\omega_l \delta t/2) \cos(\Omega \delta t/2) - \Delta \cos(\omega_l \delta t/2) \sin(\Omega \delta t/2)}{\Omega \cos(\omega_l \delta t/2) \cos(\Omega \delta t/2) + \Delta \sin(\omega_l \delta t/2) \sin(\Omega \delta t/2)}. \quad (S3)$$

When the laser detuning vanishes ($\Delta = 0$) we obtain $\phi = \omega_l \delta t = \omega \delta t$. Similarly, if $\Omega_R \rightarrow 0$, the phase ϕ converges to $\omega \delta t$. In the regime with $|\Delta| \gg |\Omega_R|$ where $\Omega = \sqrt{\Omega_R^2 + \Delta^2} \approx \Delta + \frac{\Omega_R^2}{2\Delta}$, the effects of the laser field can be characterized by the AC-Stark shift $\omega_{ac} = \frac{\Omega_R^2}{4\Delta}$, so that we obtain

$$\begin{aligned} \tan(\phi/2) &\approx \frac{\Delta \sin(\omega_l \delta t/2) - (\Delta + \frac{\Omega_R^2}{2\Delta})\delta t/2 + \frac{\Omega_R^2}{2\Delta} \sin(\omega_l \delta t/2) \cos((\Delta + \frac{\Omega_R^2}{2\Delta})\delta t/2)}{\Delta \cos(\omega_l \delta t/2) - (\Delta + \frac{\Omega_R^2}{2\Delta})\delta t/2 + \frac{\Omega_R^2}{2\Delta} \cos(\omega_l \delta t/2) \cos((\Delta + \frac{\Omega_R^2}{2\Delta})\delta t/2)} \\ &\approx \tan\left(\left(\omega - \frac{\Omega_R^2}{2\Delta}\right)\delta t/2\right). \end{aligned} \quad (S4)$$

Therefore the phase acquired during the excitation is given by the AC-Stark-shifted phase-evolution

$$\phi \approx (\omega - 2\omega_{ac}) \delta t. \quad (S5)$$

If the interactions among the atoms are neglected during the ps pulses, this intrapulse phase is common to the higher- and lower-density ensembles under the condition that their sizes, shapes and relative position are identical. Accordingly, the intrapulse phase is cancelled out in the phase-shift between those two ensembles. However, the interactions could make the intrapulse phase different between the higher- and lower-density ensembles, and that difference could appear as the zero-delay offset in the phase-shift. Also slight differences in the sizes, shapes and relative position between the higher- and lower-density ensembles, even without considering interactions, can contribute to the constant phase offset (see Methods).

MEAN-FIELD MODEL

For the mean field approximation we follow the notation $|e\rangle_j \langle e|_j = P_{ee}^{(j)}$ which results in

$$\hat{H} = \sum_{j=1}^N E_e P_{ee}^{(j)} + \sum_{j=1}^{N-1} \sum_{i>j}^N U(r_{i,j}) P_{ee}^{(i)} P_{ee}^{(j)}. \quad (\text{S6})$$

Without loss of generality we have set $E_g = 0$. By using $P_{ee}^{(j)} = \langle P_{ee}^{(j)} \rangle + \delta P_{ee}^{(j)}$ we obtain the meanfield approximation from

$$\begin{aligned} P_{ee}^{(i)} P_{ee}^{(j)} &\approx \langle P_{ee}^{(i)} \rangle \langle P_{ee}^{(j)} \rangle + \langle P_{ee}^{(i)} \rangle \delta P_{ee}^{(j)} + \langle P_{ee}^{(j)} \rangle \delta P_{ee}^{(i)} \\ &= \langle P_{ee}^{(i)} \rangle P_{ee}^{(j)} + \langle P_{ee}^{(j)} \rangle P_{ee}^{(i)} - \langle P_{ee}^{(i)} \rangle \langle P_{ee}^{(j)} \rangle, \end{aligned} \quad (\text{S7})$$

which allows to write the Hamiltonian in the following form

$$\begin{aligned} \hat{H} &= \sum_{j=1}^N \hat{H}_j \\ &= \sum_{j=1}^N \hbar \left(\omega + \left(\langle P_{ee} \rangle - \frac{\langle P_{ee} \rangle^2}{2} \right) \Delta\omega_j \right) P_{ee}^{(j)} - \hbar \left(\frac{\langle P_{ee} \rangle^2}{2} \Delta\omega_j \right) P_{gg}^{(j)}. \end{aligned} \quad (\text{S8})$$

Each atom can be considered separately, and the interactions enter as shifts of the energy levels with $\hbar \left(\langle P_{ee} \rangle - \frac{\langle P_{ee} \rangle^2}{2} \right) \Delta\omega_j$ and $\hbar \left(\frac{\langle P_{ee} \rangle^2}{2} \Delta\omega_j \right)$ for the Rydberg and ground states, respectively. Here $\Delta\omega_j = \sum_{j \neq i} U(r_{i,j})/\hbar$ is the sum over all interactions with atom ‘j’.

The interferogram obtained in the Ramsey measurement is the average over the interferograms from all the atoms shined with the ps pulses and is given by

$$P_{\text{mf}}(\tau) = \frac{1}{N} \sum_{j=1}^N P_{\text{mf};j}(\tau) = 2p_g p_e \left(1 + \frac{1}{N} \sum_{j=1}^N \cos((\omega + p_e \Delta\omega_j)\tau + \phi) \right). \quad (\text{S9})$$

By employing the Monte Carlo method to model a realistic distribution of the N atoms as given by Eq. (S18) we acquire the results of Eq. (S9).

ANALYTIC RAMSEY MODEL (ARM)

For two interacting atoms described by the Hamiltonian in Eq. (3) with $N = 2$ the time-domain Ramsey signal from each atom can be obtained by a direct calculation of the temporal evolution of the system. For example the signal from the first atom, indexed by $j = 1$ without loss of generality, is derived from $|\psi(\tau)\rangle = (A \otimes A) \exp(-iH\tau/\hbar)(A \otimes A)|gg\rangle$ as

$$\begin{aligned} P_{1(2)}(\tau) &= \langle \psi(\tau) | e \rangle_1 \langle e |_1 \psi(\tau) \rangle \\ &= 2p_g p_e (1 + p_g \cos(\omega\tau + \phi) + p_e \cos((\omega + \Delta)\tau + \phi)). \end{aligned} \quad (\text{S10})$$

For three and four interacting atoms, respectively, the relevant signals can be obtained similarly as

$$P_{1(3)}(\tau) = 2p_g p_e \left(1 + p_g^2 \cos(\omega\tau + \phi) + p_g p_e (\cos((\omega + \Delta_{12})\tau + \phi) + \cos((\omega + \Delta_{13})\tau + \phi)) + p_e^2 \cos((\omega + \Delta_{12} + \Delta_{13})\tau + \phi) \right), \quad (\text{S11})$$

$$P_{1(4)}(\tau) = 2p_g p_e \left(1 + p_g^3 \cos(\omega\tau + \phi) + p_g^2 p_e (\cos((\omega + \Delta_{12})\tau + \phi) + \cos((\omega + \Delta_{13})\tau + \phi) + \cos((\omega + \Delta_{13})\tau + \phi)) + p_g p_e^2 (\cos((\omega + \Delta_{12} + \Delta_{13})\tau + \phi) + \cos((\omega + \Delta_{12} + \Delta_{14})\tau + \phi) + \cos((\omega + \Delta_{13} + \Delta_{14})\tau + \phi)) + p_e^3 (\cos((\omega + \Delta_{12} + \Delta_{13} + \Delta_{14})\tau + \phi)) \right). \quad (\text{S12})$$

Extrapolating these procedures to N interacting atoms, the signal from the first atom interacting with the other $N - 1$ atoms is given without loss of generality by

$$P_{1(N)}(\tau) = 2p_g p_e \left[1 + p_g^{(N-1)} \cos(\omega\tau + \phi) + p_g^{(N-2)} p_e \left(\sum_{i_1=2}^N \cos((\omega + \Delta_{1i_1})\tau + \phi) \right) + p_g^{(N-3)} p_e^2 \left(\sum_{i_1=2}^{N-1} \sum_{i_2>i_1}^N \cos((\omega + \Delta_{1i_1} + \Delta_{1i_2})\tau + \phi) \right) + \dots + p_e^{N-1} \left(\sum_{i_1=2}^{N-(N-2)} \dots \sum_{i_{(N-1)}>i_{(N-2)}}^N \cos((\omega + \Delta_{1i_1} + \Delta_{1i_2} + \Delta_{1i_3} + \dots + \Delta_{1i_{(N-1)}})\tau + \phi) \right) \right], \quad (\text{S13})$$

where $\Delta_{ij} = U(r_{i,j})/\hbar$ describes an interaction-induced frequency shift between two atoms labeled by their index values i and j . Hereafter we will abbreviate $P_{1(N)}$ by P_1 . Setting $\Delta_{ij} = 0$ reduces the sums to binomial coefficients and results in the standard expression for the Ramsey signal without interactions $P_1(\tau) = 2p_g p_e (1 + \cos(\omega\tau + \phi))$.

For a large atom number N the sums can be substituted by integrals and we obtain oscillation terms given by

$$\begin{aligned} B_1 &= \sum_{i_1=2}^N \cos((\omega + U(r_{1,i_1})/\hbar)\tau + \phi) = \Re \left\{ e^{i(\omega\tau + \phi)} \int dV f_1(r, \theta, \hat{\phi}) e^{i\frac{U(r)}{\hbar}\tau} \right\}, \quad (\text{S14}) \\ B_2 &= \sum_{i_1=2}^{N-1} \sum_{i_2>i_1}^N \cos((\omega + U(r_{1,i_1})/\hbar + U(r_{1,i_2})/\hbar)\tau + \phi) \\ &= \Re \left\{ e^{i(\omega\tau + \phi)} \iint dV_1 dV_2 f_2(r_1, r_2, \theta_1, \theta_2, \hat{\phi}_1, \hat{\phi}_2) e^{i\left(\frac{U(r_1) + U(r_2)}{\hbar}\right)\tau} \right\}, \\ B_3 &= \dots \end{aligned}$$

The function f_m is related to the distribution that describes the probability to find m atoms in the ensemble where atom 1 is excluded. For example, the function f_2 is a conditional distribution where the position of the second atom depends on the position of the first one. These functions follow the condition

$$\int \dots \int dV_1 \dots dV_m f_m = \binom{N-1}{m}, \quad (\text{S15})$$

where $\binom{N-1}{m}$ describes a binomial coefficient. They depend on the geometric profile of the atom ensemble which is determined by the density function $n(\mathbf{x})$.

For a big ensemble with a large number of atoms N , where the density can be considered to be homogeneous in a small volume around a particular location (Supp. Fig. 2), we can approximate the function f_m locally by a constant value $f_m \approx \left(\frac{3}{4\pi r_0^3}\right)^m \binom{N_0-1}{m}$. Here r_0 is the cutoff radius, and $N_0 - 1$ is the number of atoms surrounding the central atom '1' in the local volume $V = \frac{4\pi r_0^3}{3}$.

This is not an oversimplification of the general problem where all the interactions of one atom with any other atoms in the ensemble have to be considered to calculate the modulation of its Ramsey signal. This simplification is justified by the fact that we observe the atomic ensemble only through a certain time window (~ 500 ps) after the initialization

by the first excitation in our experiment. Since the interaction strength decreases as the distance from the atom 1 becomes larger, atoms beyond a certain radius do not contribute to the modulation of the Ramsey signal in this time window and become only relevant to the modulation at later times.

The identity $p_g + p_e = 1$ and the convergence of the Ramsey signal for distances $r \geq r_0$ allow us to substitute N by N_0 , which leads to

$$\begin{aligned} P_1(\tau) &= 2p_g p_e \Re \left\{ 1 + e^{i(\omega\tau + \phi)} \sum_{m=0}^{N_0-1} \binom{N_0-1}{m} p_g^{(N_0-m-1)} p_e^m \left(\left(\frac{3}{r_0^3 - r_B^3} \right) \int_{r_B}^{r_0} dr r^2 e^{i(U(r)/\hbar)\tau} \right)^m \right\} \\ &= 2p_g p_e \Re \left\{ 1 + e^{i(\omega\tau + \phi)} \left(p_g + p_e \left(\frac{3}{r_0^3 - r_B^3} \right) \int_{r_B}^{r_0} dr r^2 e^{i(U(r)/\hbar)\tau} \right)^{N_0-1} \right\} \\ &= 2p_g p_e \Re \left\{ 1 + e^{i(\omega\tau + \phi)} (p_g + p_e \gamma(\tau))^{N_0-1} \right\} \end{aligned} \quad (\text{S16})$$

for the atom 1. The radius r_B emerges from the limited bandwidth of the pump excitation and is equivalent to the Rydberg-blockade radius.

To obtain the result averaged over the atomic ensemble containing millions of atoms one needs to evaluate the following summation

$$\begin{aligned} P(\tau) &= \frac{1}{N} \sum_{j=1}^N P_j(\tau) \\ &= 2p_g p_e \Re \left\{ 1 + \frac{1}{N} e^{i(\omega\tau + \phi)} \sum_{j=1}^N (p_g + p_e \gamma(\tau))^{N_0(\mathbf{x}_j)-1} \right\}, \end{aligned} \quad (\text{S17})$$

where the number of atoms N_0 depends on the local density due to $N_0(\mathbf{x}_j) = \frac{4\pi(r_0^3 - r_B^3)}{3} n(\mathbf{x}_j)$.

The density distribution of our atomic ensemble can be modeled by a Gaussian distribution of the following form

$$n(\mathbf{x}) = n_p e^{-\frac{(x^2+y^2)}{2\sigma_{xy}^2} - \frac{z^2}{2\sigma_z^2}}, \quad (\text{S18})$$

where $n_p = \frac{N}{(2\pi)^{3/2} \sigma_{xy}^2 \sigma_z}$ is the peak density, and σ_{xy} is the width in the x,y-direction and σ_z is the width in the z-direction of the atomic ensemble. This allows us to exchange the summation over the atom number in Eq. (S17) by an integral form given by

$$P(\tau) = 2p_g p_e \Re \left\{ 1 + \frac{4\pi}{N} e^{i(\omega\tau + \phi)} \int_0^\infty d\rho \rho^2 n(\rho) (p_g + p_e \gamma(\tau))^{N_0(\rho)-1} \right\}, \quad (\text{S19})$$

where the radius ρ is defined by $\rho = \sqrt{x^2 + y^2 + \left(z \frac{\sigma_{xy}}{\sigma_z} \right)^2}$. This formulation can be further simplified by exchanging the integral over the volume of the ensemble by an integral over the density to yield

$$P(\tau) = 2p_g p_e \Re \left\{ 1 + \frac{2}{\sqrt{\pi} n_p} e^{i(\omega\tau + \phi)} \int_0^{n_p} dn \sqrt{\ln \left(\frac{n_p}{n} \right)} (p_g + p_e \gamma(\tau))^{N_0(n)-1} \right\}, \quad (\text{S20})$$

in which the Ramsey contrast and phase can be derived from

$$\begin{aligned} g(\tau) &= |g(\tau)| e^{i\alpha(\tau)} \\ &= \frac{2}{\sqrt{\pi} n_p} \int_0^{n_p} dn \sqrt{\ln \left(\frac{n_p}{n} \right)} (p_g + p_e \gamma(\tau))^{N_0(n)-1} \end{aligned} \quad (\text{S21})$$

to be the absolute value and phase of the function $g(\tau)$, respectively.

In the case that the potential is given by a dipole-dipole (DD) interaction $U(r) = C_3/r^3$, a van der Waals (vdW) interaction $U(r) = C_6/r^6$ or a hybrid form of these two (Eff. Potential) as presented in Eq. (S25) in the next paragraph, the term $(p_g + p_e \gamma(\tau))^{N_0-1}$ from Eq. (S16) can be simplified even further by taking N_0 to infinity. Here, we obtain

$$\left| \lim_{N_0 \rightarrow \infty} (p_g + p_e \gamma(\tau))^{N_0-1} \right| \approx \begin{cases} e^{-\kappa\tau} & \text{DD} \\ e^{-\sigma\sqrt{\tau}} & \text{vdW} \\ e^{-\frac{2}{\pi}\kappa\tau \left(\frac{\pi}{2} - \text{Si}(\omega_c\tau) \right) - \sqrt{\frac{8}{\pi}} \sigma\sqrt{\tau} S(\sqrt{\omega_c\tau})} & \text{Eff.Potential} \end{cases} \quad (\text{S22})$$

with the decay constants $\kappa = p_e \frac{2\pi^2 C_3}{3\hbar} n$ for a dipole-dipole interaction and $\sigma = p_e \frac{\pi}{3} \sqrt{\frac{8\pi C_6}{\hbar}} n$ for a van der Waals interaction. $\hbar\omega_c = \frac{C_3}{r_c^3} = \frac{C_6}{r_c^6}$ is the potential energy at the crossover radius r_c and $\text{Si}(x) = \int_0^x dt \sin(t)/t$ and $S(x) = \int_0^x dt \sin(t^2)$ is the Sine and Fresnel sine integral, respectively.

The corresponding phase shift for $\lim_{N_0 \rightarrow \infty} (p_g + p_e \gamma(\tau))^{N_0-1}$ in the case of a van der Waals or an effective interaction is given by

$$\Phi_{\text{vdW}}(\tau) = \sigma \sqrt{\tau} \quad (\text{S23})$$

$$\Phi_{\text{Eff}}(\tau) = \left(-\frac{2}{\pi} \kappa \tau \text{Ci}(\omega_c \tau) + \sqrt{\frac{8}{\pi}} \sigma \sqrt{\tau} C(\sqrt{\omega_c \tau}) \right), \quad (\text{S24})$$

where $\text{Ci}(x) = -\int_x^\infty dt \cos(t)/t$ and $C(x) = \int_0^x dt \cos(t^2)$ is the Cosine and Fresnel cosine integral, respectively. The phase shift in the case of the van der Waals interaction is equal to its decay constant times the square root of the pump-probe delay τ . On the other hand, the phase shift for a pure dipole-dipole interaction is divergent when N_0 approaches infinity. It is interesting to note that the characteristic decay signal for a van der Waals interaction is given by an exponential function where the square root of the pump-probe delay τ enters in the argument. On the other hand, for the dipole-dipole interaction the decay is given by an exponential function where the pump-probe delay τ appears as a linear term in the argument.

EFFECTIVE INTERACTION AND INTERACTION ANISOTROPY

The dipole-dipole interaction enters solely in the non-diagonal terms of the Hamiltonian, coupling the initial Rydberg states of a pair of atoms described by $|\dots e \dots e \dots\rangle$ to other Rydberg states $|\dots e' \dots e'' \dots\rangle$. Such couplings induce hybridization among multiple Rydberg states, leading to congested potential structures.

To handle this intractable problem we define a single effective potential for the two-atom interaction that represents the congested potential structure. Thereby, the effective interaction enters only in the diagonal components of the Hamiltonian. At short interatomic distances this effective potential is of dipolar character which changes continuously into a van der Waals potential at larger interatomic distances.

In the main text we have considered the effective potential

$$U(r) = \begin{cases} -\frac{C_3}{r^3} & r \leq r_c \\ -\frac{C_6}{r^6} & r > r_c \end{cases} \quad (\text{S25})$$

without an anisotropy for the mean-field and ARM simulations with the Hamiltonian in Eq. (3).

Here we introduce anisotropies into the dipole-dipole and van der Waals interactions:

$$U(r, \theta) = \begin{cases} -\frac{C_3 |1 - 3 \cos^2(\theta)|}{r^3} & r \leq r_c(\theta) \\ -\frac{C_6 (1 - 3 \cos^2(\theta))^2}{r^6} & r > r_c(\theta) \end{cases} \quad (\text{S26})$$

where θ is the angle between the z-axis shown in Fig. 1a and a line connecting two atoms interacting with each other. The continuity of the interaction strength at $\theta = 0$ gives $C_6 = \frac{C_3 (r_c(0)^3)^2}{2}$. Similarly the continuity at the crossover radius r_c gives

$$r_c(\theta) = r_c(0) \sqrt[3]{\frac{|1 - 3 \cos^2(\theta)|}{2}}. \quad (\text{S27})$$

It should be noted that r_c is not defined at $\theta = 54.7$ and 125.3 degrees as the interaction vanishes.

The comparisons between our experimental observations and the simulations with the anisotropic potential $U(r, \theta)$ above are presented in Supp. Fig. 3 for the mean field model and in Supp. Fig. 4 for our ARM, respectively. It is seen in Supp. Figs. 3c and d that the mean-field simulations clearly fail to reproduce the observed phase-shifts again, whereas the ARM simulations agree reasonably with the measured Ramsey contrasts and phase-shifts for both of the Rydberg populations $p_e \sim 1.2\%$ to 3.3% . The adjustment parameters employed in these ARM simulations are $C_3 = 5.8 \text{ GHz } \mu\text{m}^3$ and $r_c = 2.7 \mu\text{m}$ and are comparable to $C_3 = 4.3 \text{ GHz } \mu\text{m}^3$ and $r_c = 1.95 \mu\text{m}$ employed in the simulations without the potential anisotropy in the main text.

We have also performed simulations with a pure dipolar and van der Waals potentials without anisotropies as presented in Supp. Fig. 5 for the mean field model and in Supp. Fig. 6 for our ARM, respectively. It is seen in

Supp. Figs. 5c and d that the mean-field simulations fail to reproduce the observed phase-shifts again for both the pure dipolar and van der Waals potentials. The ARM simulations with the pure van der Waals potential, on the other hand, show reasonable agreements simultaneously with the Ramsey contrasts and phase-shifts, whereas similar reasonable agreements have not been found with the pure dipolar potential. Supplementary Figure 7 shows the two-atom potentials that we have obtained by diagonalizing the ^{87}Rb Hamiltonian for two atoms with the dipole-dipole interaction. It is seen from this figure that the van der Waals interaction is unreasonable at interatomic distances shorter than $3\ \mu\text{m}$, which is one-order longer than the shortest interatomic distance $r_{\text{B}} \sim 0.39\ \mu\text{m}$ in our observation with the 75 GHz half-bandwidth of the ps pulse excitation. These simulations with the pure dipolar and van der Waals potentials and their relevant discussion thus necessitates the potential presented in Eq. (S25) or Eq. (S26).

Supplementary Figure 8 shows the Ramsey contrast and the phase-shift at $\tau = 500$ ps simulated by ARM without potential anisotropies with the population of the $42\text{D}_{5/2}$ being $\sim 3.3\%$ and plotted as functions of the cutoff radius r_0 (the lower abscissa), at which we truncate the integration in Eq. (6), and of the average atom number within the volume $V = \frac{4\pi}{3}(r_0^3 - r_{\text{B}}^3)$ (the higher abscissa). The Ramsey contrast and phase-shift simulated with the pure van der Waals potential converge similarly to those simulated with the potential in Eq. (S25) in the main text. The converged values agree well with the measured ones indicated by the dark-gray solid lines, each of which is the average over eight points around $\tau=500$ ps in Fig. 4b or d. The light-gray shaded area represents one standard deviation of the average over those eight measured values. It should be noted here again that the pure van der Waals potential is unreasonable, as described above, even though it gives the ARM simulations in reasonable agreement with the experimental observations. On the other hand, the Ramsey contrast and phase-shift simulated with the pure dipolar potential do not converge clearly and disagree with the experimental observations. The black solid line in Supp. Fig. 8a shows the Ramsey contrast $|g(\tau)|$ given by Eq. (S21) with $\gamma(\tau) = 0$, which gives the situation where the Ramsey oscillations modulated by the Rydberg-Rydberg interactions are dephased completely. This black solid line thus represents the upper limit of the contrast decay and accordingly the lower limit of the number of atoms ~ 32 to reproduce the Ramsey contrast ~ 0.45 measured at $\tau = 500$ ps, irrespective of the potential curves.

FIELD IONIZATION SPECTRA AND ESTIMATION OF EXCITATION BANDWIDTH

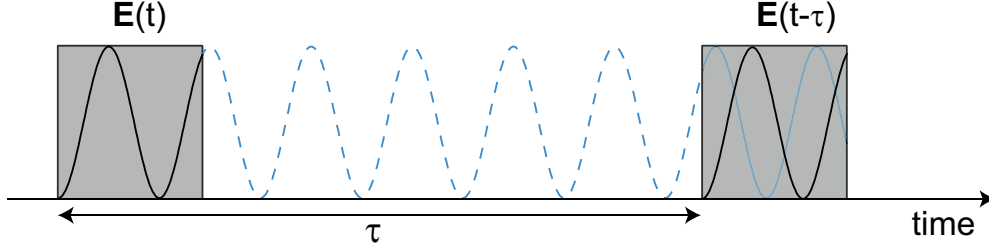
In order to reduce the number of Rydberg states to be excited, the spectra of the ps IR and blue pulsed lasers were cut to be about 0.13 nm and 0.20 nm, respectively, with pulse shapers in a 4f configuration ($f=500$ mm). These bandwidths were common to the Ramsey measurements of the three different Rydberg states $\nu=38, 42,$ and 50 . Supplementary Figure 9a shows state-resolved field-ionization spectra measured by ramping the electric field slowly on the microsecond timescale. The spectra indicate that a single state is predominantly populated for each of the excitations to $\nu=38$ and 42 , as seen in Supp. Fig. 9a, whereas more levels are populated for the excitation to $\nu=50$, as seen in Supp. Fig. 9b. This is because the energy levels of Rydberg states are inversely dependent on ν^2 and more congested for higher states. Due to the characteristics of field ionization, the threshold value of the electric field to induce ionization depends on ν^{-4} (Ref. 11), so that higher states are less resolvable with the same ramp-up speed of the electric field. Therefore the ramp-up speed is slower for $\nu=50$ than for $\nu=38$ and 42 by a factor of $2/3$.

The bandwidth of our Rydberg excitation with the IR and blue pulses was determined from the field-ionization spectrum for $\nu=42$ presented in Fig. 1c as well as in Supp. Fig. 9a. Assuming a symmetrical population distribution with respect to the center level $\nu = 42$, we estimated the relative populations in the excited Rydberg states to be $\sim 84\%$ for the center state 42D and $\sim 8\%$ for each neighboring state 43D and 41D , respectively, from the integrated areas of the ion signal peaks. In Supp. Fig. 9a, the integration range for the 43D state (the 42D and 41D states) is indicated by the red-shaded (blue-shaded) region. We did not deconvolute the ion spectrum for those integrations although those peaks were not fully resolved. Based on the relative populations and assuming a Gaussian excitation spectrum, we obtained a bandwidth of ~ 150 GHz (FWHM).

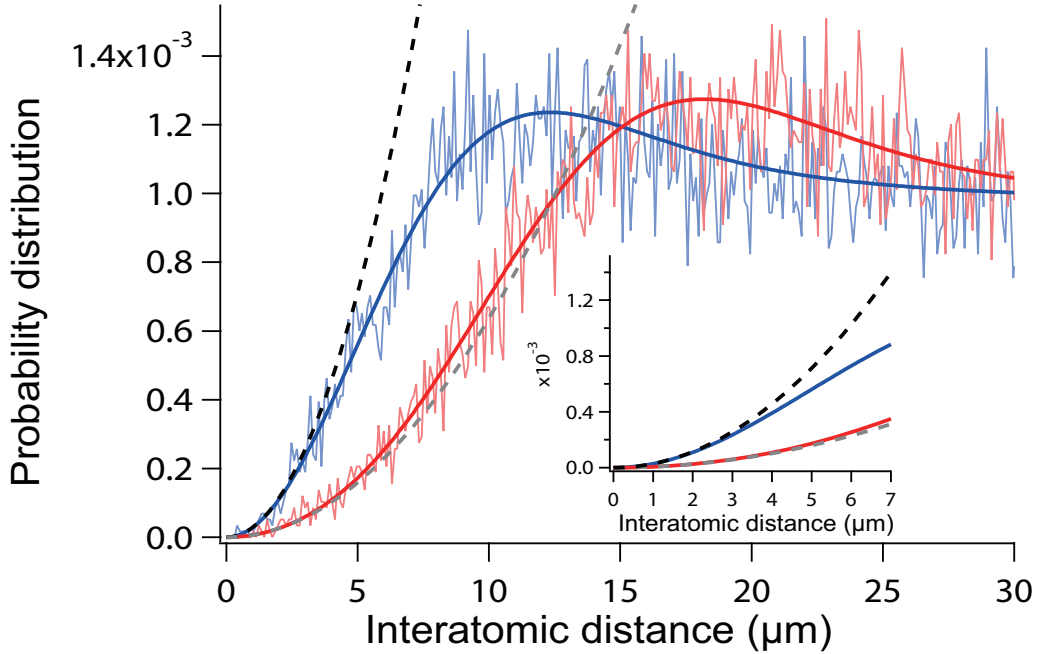
ATOM-DENSITY DEPENDENCE OF THE RAMSEY-CONTRAST DECAY

We have measured the Ramsey contrasts for $\nu=42$ with a population of $3.5\pm 0.3\%$ at $\tau = 300$ and 510 ps for several different atom densities ranging from the lower to the higher densities described in the main text. These measurements were made by changing the power of the dipole-trap laser and thereby the trap depth. At first the atom densities in these Ramsey measurements were estimated solely from the total number of atoms and the size of the atomic ensemble obtained by in-situ absorption imaging with a CCD camera without expanding the atomic ensemble, but were underestimated because of the spatial resolution of the CCD camera, as is described in the subsection ‘‘Estimation

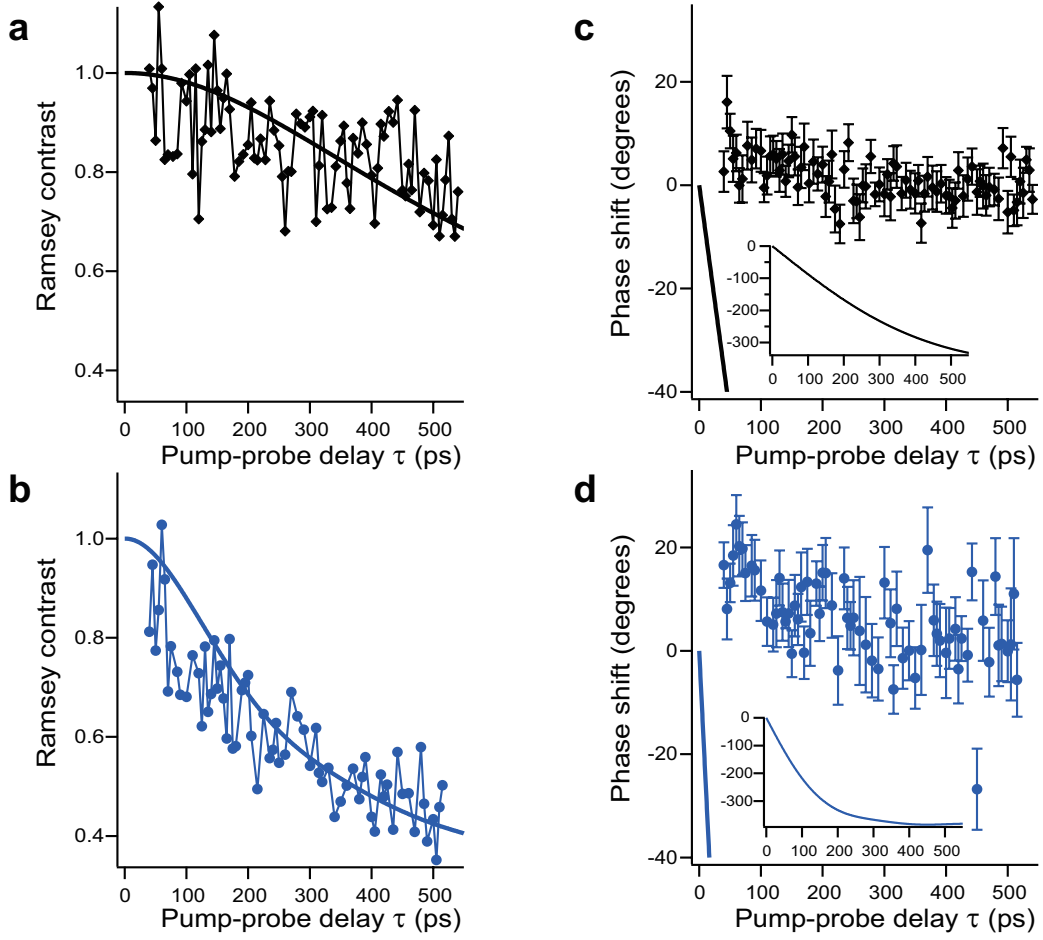
of the atom density” in Methods. Therefore it was calibrated in a later independent experiment in which the trapping conditions (1) and (3) (the loading sequence and the dipole-trap laser focusing), which were described in the subsection “Estimation of the atom density” in Methods, were almost the same as those employed in the Ramsey measurements. In this calibration experiment, we measured the radial trap-frequency, the temperature, the axial size, and the total number of atoms to obtain the atom density as a function of the power of the dipole-trap laser. Supp. Fig. 10 shows the results of this calibration measurement accompanied by a calibration curve, which is a linear interpolation function. The atom densities in the Ramsey measurements are estimated from this calibration curve as a function of the dipole-trap-laser power as shown by the blue diamond-shaped data points in Supp. Fig. 10, and then the Ramsey contrasts measured at $\tau = 300$ and 510 ps are plotted against these estimated atom densities in Supp. Fig. 11. It is seen in Supp. Fig. 11 that the contrast decay is accelerated as the atom density is increased.



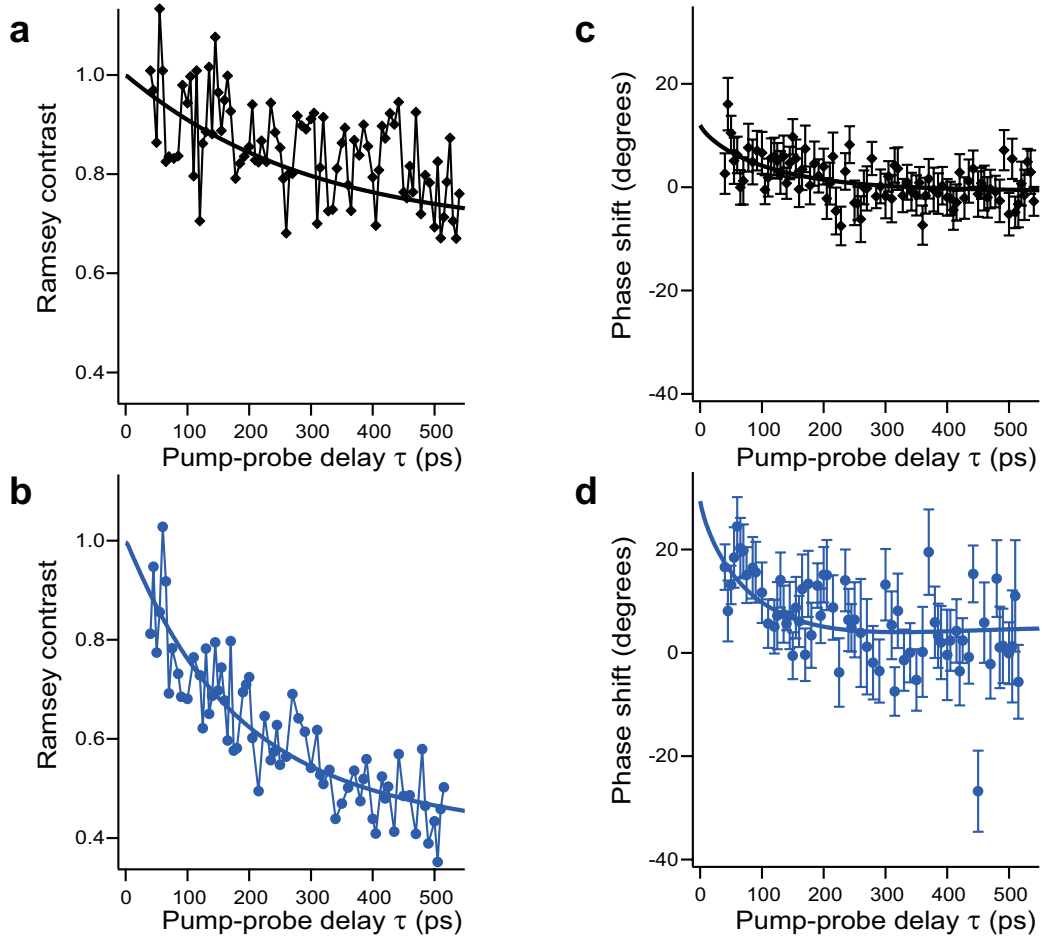
Supplementary Figure 1: Schematic of a pulse sequence in Ramsey interferometry. The black and blue solid lines stand for the CEPs of the pump and probe pulses, whose pulse-envelopes are assumed to be rectangle for simplicity, in the time-domain and frequency-domain Ramsey interferometry, respectively.



Supplementary Figure 2: Distribution of the interatomic distance. The blue and red solid lines show two examples of the distance distribution, in each of which the noisy line is obtained by a Monte-Carlo simulation, and the smooth line by numerical calculations considering the atom density given by Eq. (S18). The blue solid lines show the distance distributions from the perspective of the central location $\mathbf{x} = 0$ in the ensemble, around which we set the peak atom density to $\sim 1.3 \times 10^{12} \text{ cm}^{-3}$, whereas the red solid lines show the distributions from the perspective of an off-center location $\mathbf{x} = [7 \mu\text{m}, 7 \mu\text{m}, 250 \mu\text{m}]$, around which the density is $\sim 2.9 \times 10^{11} \text{ cm}^{-3}$. The black and gray dashed lines represent the distance distributions for homogeneous density distributions assumed locally around those two locations. It is seen in the inset that they agree reasonably with the numerical ones for the distance shorter than $\sim 4 \mu\text{m}$. Those distance distributions with locally homogeneous densities have been employed in the ARM simulations of the Ramsey signals.

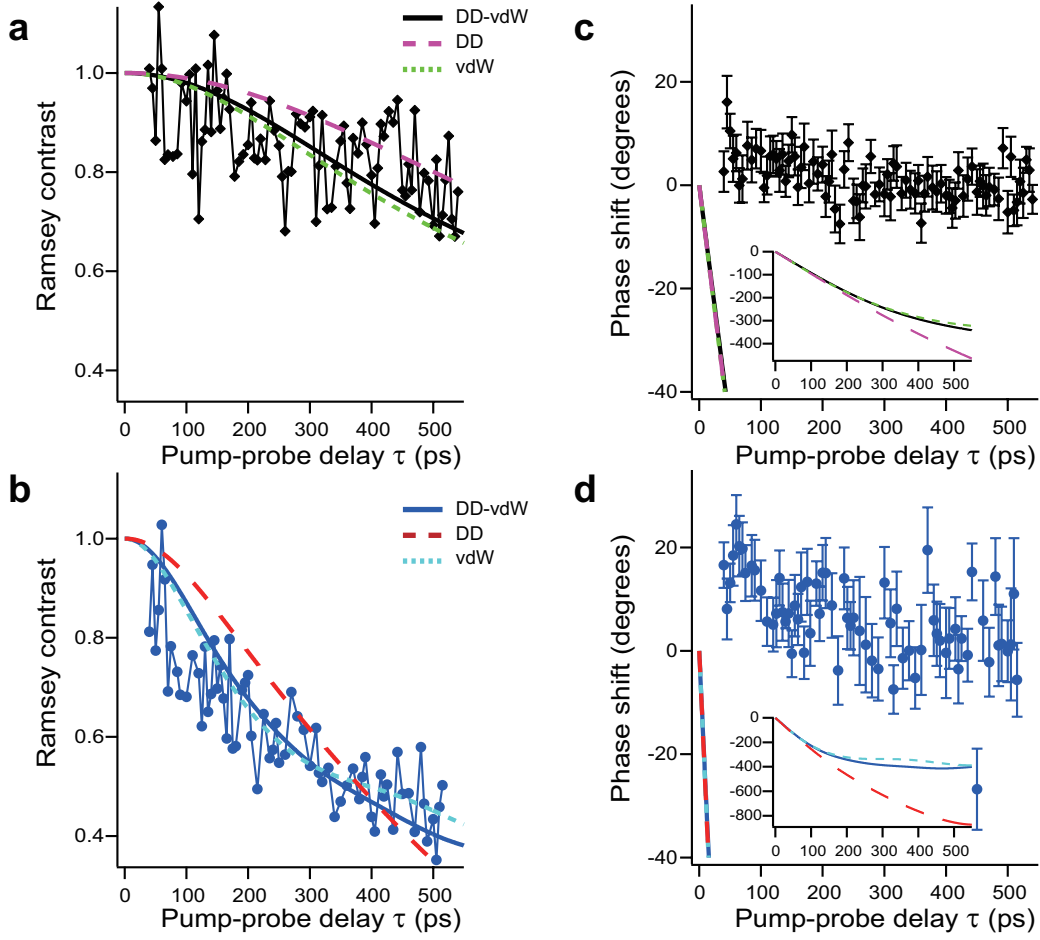


Supplementary Figure 3: Mean-field analysis of the Ramsey contrast and the phase shift with a potential anisotropy. The black-diamond-shaped and blue-circle data-points show the Ramsey contrasts (**a** and **b**) and the phase-shifts (**c** and **d**) measured with the population of the $42D_{5/2}$ state being $\sim 1.2\%$ (**a** and **c**) and $\sim 3.3\%$ (**b** and **d**), respectively. In **a** and **b**, the Ramsey contrasts simulated by mean-field theory with the anisotropic potential given by Eq. (S26) (black and blue solid lines) are compared with the measured ones. Similarly, the measured and simulated phase-shifts are compared in **c** and **d**. The insets in **c** and **d** show the whole features of the simulated phase-shifts by reducing their vertical scalings. The zero-delay offset of the simulated phase-shift is arbitrary and set to 0 degree. The interaction strength is limited below 75 GHz, which is the bandwidth (half width half maximum) of the pump excitation, and the peak atom density is set to $\sim 1.3 \times 10^{12} \text{ cm}^{-3}$ in these simulations. The coefficient $C_3 = 4.1 \text{ GHz}\mu\text{m}^3$ and the crossover radius $r_c = 1.1 \mu\text{m}$ have been used in these simulations.

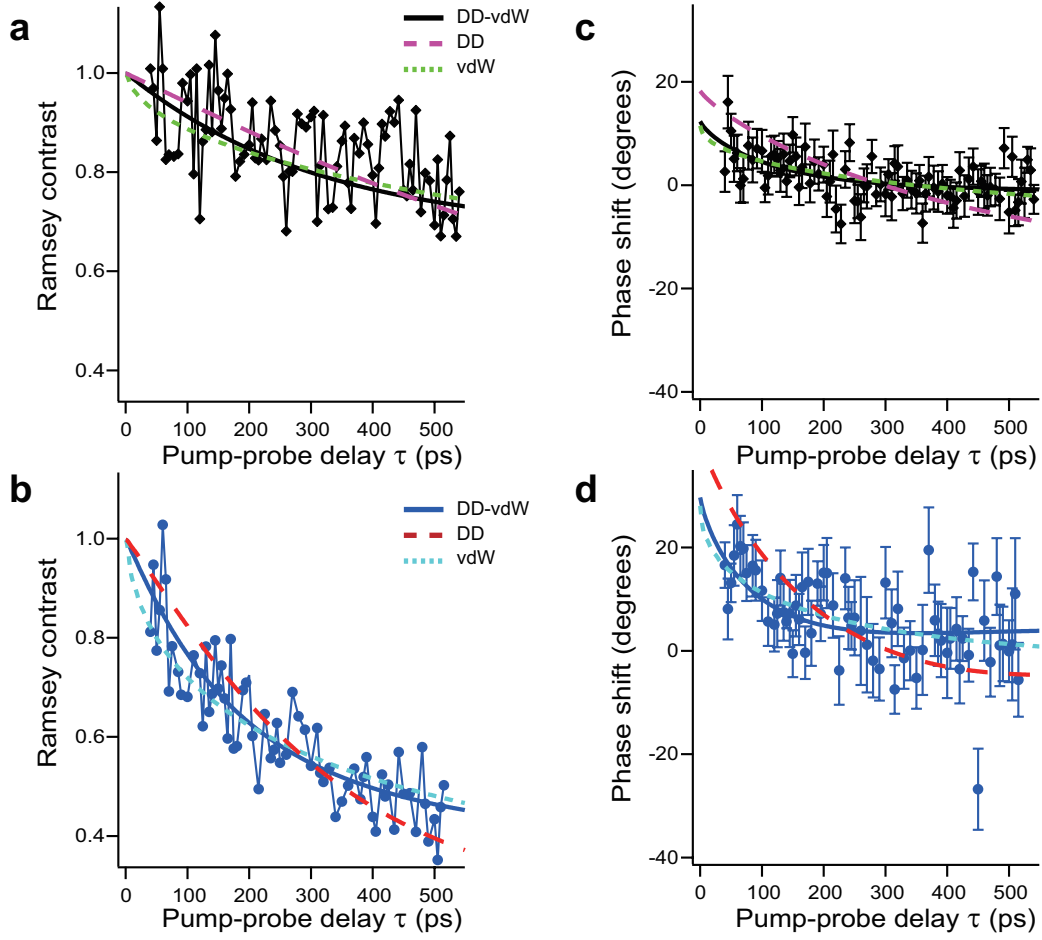


Supplementary Figure 4: ARM analysis of the Ramsey contrast and the phase shift with a potential anisotropy.

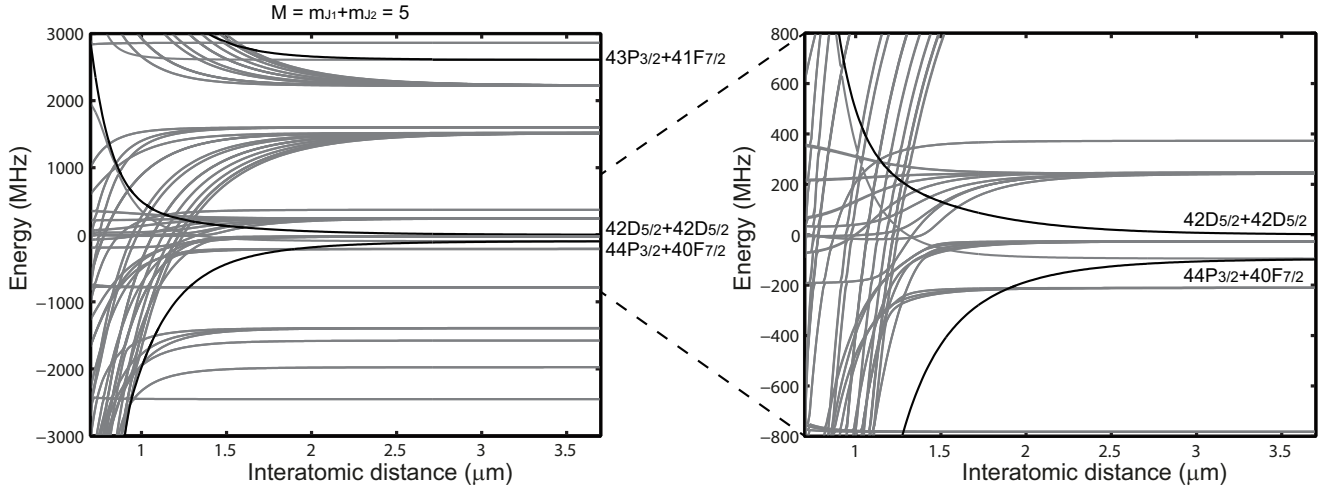
The black-diamond-shaped and blue-circle data-points show the Ramsey contrasts (**a** and **b**) and the phase-shifts (**c** and **d**) measured with the population of the $42D_{5/2}$ state being $\sim 1.2\%$ (**a** and **c**) and $\sim 3.3\%$ (**b** and **d**), respectively. In **a** and **b**, the Ramsey contrasts simulated by ARM with the anisotropic potential given by Eq. (S26) (black and blue solid lines) are compared with the measured ones. Similarly, the measured and simulated phase-shifts are compared in **c** and **d**. The interaction strength in these simulations is limited below 75 GHz, which is the half width half maximum of the pump excitation, and the peak atom density is set to $\sim 1.3 \times 10^{12} \text{ cm}^{-3}$ in these simulations. The coefficient $C_3 = 5.8 \text{ GHz}\mu\text{m}^3$ and the crossover radius $r_c = 2.7 \mu\text{m}$ have been used in these simulations.



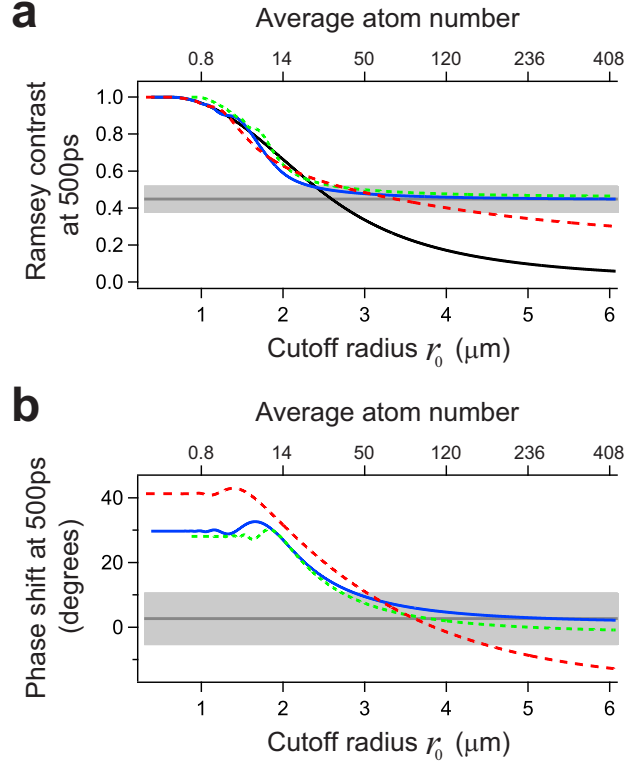
Supplementary Figure 5: Mean-field analysis of the Ramsey contrast and the phase shift with the pure dipolar and van der Waals potentials without anisotropies. The black-diamond-shaped and blue-circle data-points show the Ramsey contrasts (a and b) and the phase-shifts (c and d) measured with the population of the $42D_{5/2}$ state being $\sim 1.2\%$ (a and c) and $\sim 3.3\%$ (b and d), respectively. In a and b, the Ramsey contrasts simulated by mean-field theory with the pure dipolar (dashed line; DD) and van der Waals (dotted line; vdW) potentials without anisotropies are compared with the measured ones. Similarly, the measured and simulated phase-shifts are compared in c and d. The mean-field simulations with the potential in Eq. (S25), which have been shown in Fig. 3 in the main text, are displayed again for reference (solid line; DD-vdW). The insets in c and d show the whole features of the simulated phase-shifts by reducing their vertical scalings. The zero-delay offset of the simulated phase-shift is arbitrary and set to 0 degree. The interaction strength is limited below 75 GHz, which is the bandwidth (half width half maximum) of the pump excitation, and the peak atom density is set to $\sim 1.3 \times 10^{12} \text{ cm}^{-3}$ in these simulations. The coefficients $C_3 = 1 \text{ GHz}\mu\text{m}^3$ and $C_6 = 1.9 \text{ GHz}\mu\text{m}^6$ have been used in these simulations for the dipole-dipole and van der Waals interactions, respectively.



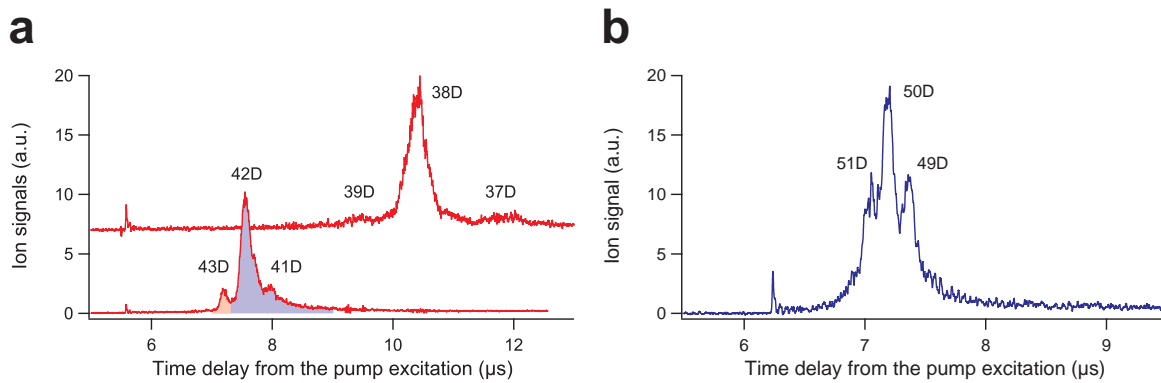
Supplementary Figure 6: ARM analysis of the Ramsey contrast and the phase shift with the pure dipolar and van der Waals potentials without anisotropies. The black-diamond-shaped and blue-circle data-points show the Ramsey contrasts (**a** and **b**) and the phase-shifts (**c** and **d**) measured with the population of the $42D_{5/2}$ state being $\sim 1.2\%$ (**a** and **c**) and $\sim 3.3\%$ (**b** and **d**), respectively. In **a** and **b**, the Ramsey contrasts simulated by ARM with the pure dipolar (dashed line; DD) and van der Waals (dotted line; vdW) potentials without anisotropies are compared with the measured ones. Similarly, the measured and simulated phase-shifts are compared in **c** and **d**. The ARM simulations with the potential in Eq. (S25), which have been shown in Fig. 4 in the main text, are displayed again for reference (solid line; DD-vdW). The interaction strength is limited below 75 GHz, which is the bandwidth (half width half maximum) of the pump excitation, and the peak atom density is set to $\sim 1.3 \times 10^{12} \text{ cm}^{-3}$ in these simulations. The coefficients $C_3 = 2.5 \text{ GHz}\mu\text{m}^3$ and $C_6 = 35 \text{ GHz}\mu\text{m}^6$ have been used in these simulations for the dipole-dipole and van der Waals interactions, respectively.



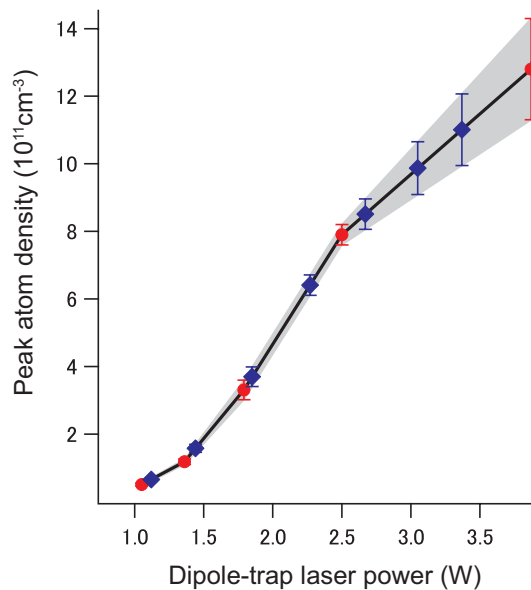
Supplementary Figure 7: Two-atom dipolar potentials around the $42D_{5/2} + 42D_{5/2}$ asymptote. $\theta = 0$ and $M = m_{J_1} + m_{J_2} = 5$, where θ is the same angle as has been used in Eq. (S26). Only the states with electronic angular momenta below $l = 5$, principal quantum numbers ranging from 38 to 46 and within ± 30 GHz from the $42D_{5/2} + 42D_{5/2}$ asymptote are considered in the diagonalization of the potential-energy matrix. The potentials that dominate the interaction between two $|42D_{5/2}, m_J = 5/2\rangle$ atoms are indicated by black solid lines.



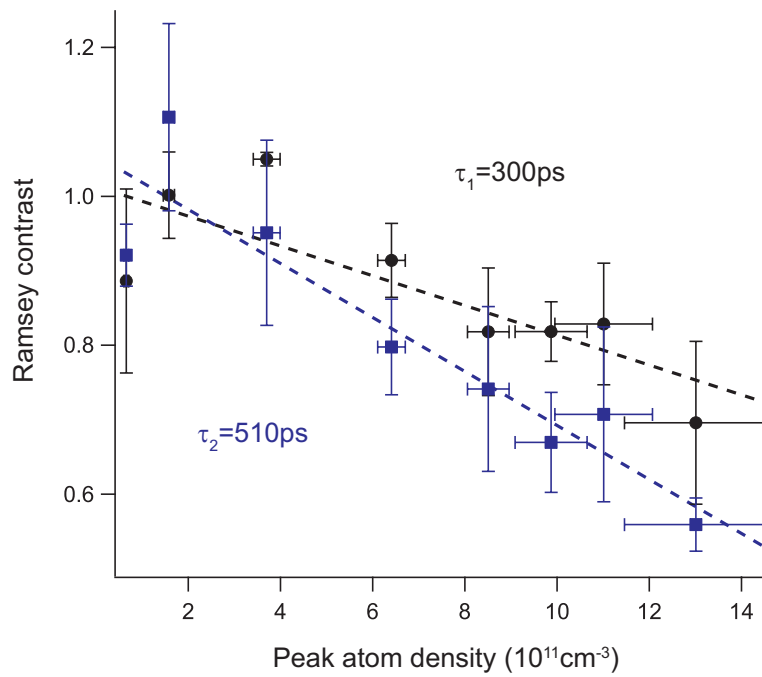
Supplementary Figure 8: Convergence of the Ramsey contrast and phase-shift simulated by ARM as functions of the cutoff radius r_0 and compared among different types of potentials without anisotropies. The Ramsey contrast and the phase-shift at $\tau = 500$ ps simulated by ARM with the population of the $42D_{5/2}$ being $\sim 3.3\%$ are plotted as functions of the cutoff radius r_0 (the lower abscissa) and the average atom number within the volume $V = \frac{4\pi}{3}(r_0^3 - r_B^3)$ (the higher abscissa). The interaction strength is limited below 75 GHz, which is the half width half maximum of the pump excitation, and the peak atom density is set to $\sim 1.3 \times 10^{12} \text{ cm}^{-3}$ in these simulations. The red dashed and green dotted lines show the results with the pure dipolar (DD) and van der Waals (vdW) potentials without anisotropies, respectively. The results with the potential in Eq. (S25), which have been shown in Fig. 5 in the main text, are displayed again for reference (blue solid line; DD-vdW). The dark-gray solid lines represent the measured Ramsey contrast and the phase-shift, each of which is the average over eight points around $\tau=500$ ps in Fig. 4b or d. The light-gray shaded area represents one standard deviation of the average over those eight measured values. The black solid line shows the Ramsey contrast $|g(\tau)|$ given by Eq. (S21) with $\gamma(\tau) = 0$, giving the upper limit of the contrast decay and accordingly the lower limit of the number of atoms ~ 32 to reproduce the Ramsey contrast ~ 0.45 measured at $\tau = 500$ ps, irrespective of the potential curves.



Supplementary Figure 9: State-resolved field-ionization spectra. **a**, Ion signals measured as functions of time-delay from the ps pulsed-laser excitations to Rydberg states $\nu = 42$ and 38. The electric field was ramped at the same speed as the one for Fig. 1c. The signal for $\nu = 38$ is shifted vertically for clarity. The atom density and Rydberg population were $\sim 4 \times 10^{10} \text{ cm}^{-3}$ and $1.2 \pm 0.1 \%$, respectively, for $\nu = 42$ and were $\sim 4 \times 10^{10} \text{ cm}^{-3}$ and $3.2 \pm 0.1 \%$, respectively, for $\nu = 38$. The red-shaded region indicates the integration range used for the estimation of the relative population in the 43D state, whereas the blue-shaded area shows the integration range for the 42D and 41D states. **b**, The ion signal for $\nu = 50$ with the atom density and Rydberg population being $\sim 3 \times 10^{10} \text{ cm}^{-3}$ and $3.1 \pm 0.2 \%$, respectively. The ramp-up speed of the electric field was slower than that for $\nu = 42$ and 38 by a factor of 2/3. The bandwidths of the excitations in these measurements in **a** and **b** are the same as the one for the pump excitation in the Ramsey measurements.



Supplementary Figure 10: The calibration of the peak atom density as a function of the power of the dipole-trap-laser. The red-circle data points show the peak atom density measured in the calibration experiment as a function of the dipole-trap-laser power. The blue-diamond-shaped data and their error bars are not measured directly, but are obtained by linear interpolation. These blue-diamond-shaped data points represent the estimated peak atom densities used in the density dependence measurement of the Ramsey contrast shown in Supp. Fig. 11. The error bars represent one standard deviations.



Supplementary Figure 11: Density dependence of the Ramsey contrast. The Ramsey contrasts are plotted as a function of the calibrated peak atom density at two different pump-probe delays $\tau=300$ and 510 ps for $\nu=42$ with its population being $\sim 3.5\%$. The vertical error bars represent one standard deviations, and the horizontal error bars correspond to the vertical error bars in Supp. Fig. 10. The dashed lines are linear fits to the measured data without considering the error bars.